

Which multiband factor should you choose for your resting-state fMRI study?

Benjamin B. Risk^{a,*}, Raphiel J. Murden^a, Junjie Wu^b, Mary Beth Nebel^{c,d}, Arun Venkataraman^e, Zhengwu Zhang^f, Deqiang Qiu^b

^a*Department of Biostatistics and Bioinformatics, Emory University*

^b*Department of Radiology and Imaging Sciences, Emory University*

^c*Center for Neurodevelopmental and Imaging Research, Kennedy Krieger Institute*

^d*Department of Neurology, Johns Hopkins University School of Medicine*

^e*Department of Physics and Astronomy, University of Rochester, Rochester, NY, United States*

^f*Department of Statistics and Operations Research, University of North Carolina at Chapel Hill, USA*

Abstract

Multiband acquisition, also called simultaneous multislice, has become a popular technique in resting-state functional connectivity studies. Multiband (MB) acceleration leads to a higher temporal resolution but also leads to spatially heterogeneous noise amplification, suggesting the costs may be greater in areas such as the subcortex. We evaluate MB factors of 2, 3, 4, 6, 8, 9, and 12 with 2 mm isotropic voxels, and additionally 2 mm and 3.3 mm single-band acquisitions, on a 32-channel head coil. Noise amplification was greater in deeper brain regions, including subcortical regions. Correlations were attenuated by noise amplification, which resulted in spatially varying biases that were more severe at higher MB factors. Temporal filtering decreased spatial biases in correlations due to noise amplification, but also tended to decrease effect sizes. In seed-based correlation maps, left-right putamen connectivity and thalamo-motor connectivity were highest in the single-band 3.3 mm protocol. In correlation matrices, MB 4, 6, and 8 had a greater number of significant correlations than the other acquisitions (both with and without temporal filtering). We recommend single-band 3.3 mm for seed-based subcortical analyses, and MB 4 provides a reasonable balance for studies analyzing both seed-based correlation maps and connectivity matrices. In multiband studies including secondary analyses of large-scale datasets, we recommend reporting effect sizes or test statistics instead of correlations. If correlations are reported, temporal filtering (or another method for thermal noise removal) should be used. The Emory Multiband Dataset is available on OpenNeuro.

Keywords: acceleration, functional connectivity, noise amplification, putamen, thalamus, simultaneous multislice, subcortical, temporal resolution

*1518 Clifton Rd NE, Atlanta, GA 30322

Email address: benjamin.risk@emory.edu (Benjamin B. Risk)

¹ **1. Introduction**

² Correlations in spontaneous blood-oxygen-level-dependent (BOLD) signal fluctuations
³ measured using resting state functional magnetic resonance imaging (rs-fMRI) are referred
⁴ to as functional connectivity, and collectively, are used to reveal the functional connectome
⁵ (Biswal et al., 2010). Patterns in functional connectivity can provide insight into the patho-
⁶ physiology of diseases, and rs-fMRI has the potential to be a biomarker of neurological and
⁷ psychiatric disorders (Greicius, 2008). In particular, functional connectivity in subcortical
⁸ regions, such as the thalamus and striatum, appears to be altered in many neurological and
⁹ psychiatric conditions (Greicius et al., 2007; Woodward and Heckers, 2016; Di Martino et al.,
¹⁰ 2011). Recently, multiband (MB) acquisition, also called simultaneous multislice, has been
¹¹ broadly adopted by large-scale efforts to map the functional connectome across all stages of
¹² human development (Glasser et al., 2013; Miller et al., 2016b; Howell et al., 2019; Weiner
¹³ et al., 2017a; Hagler et al., 2019) in part due to evidence suggesting up-to 60% increases
¹⁴ in fMRI signal fluctuation detection sensitivity (Feinberg et al., 2010). Evidence from task-
¹⁵ based fMRI data suggest the benefits of multiband acquisition may be non-uniform across
¹⁶ the brain and in some instances decline with high MB factors (Todd et al., 2017). Relatively
¹⁷ high MB factors (MB 8) are used by most of the large-scale efforts; yet, to date, the im-
¹⁸ pact of MB factor on correlation-based functional connectivity estimation has received little
¹⁹ attention.

²⁰ MB acquisition improves temporal resolution in fMRI by using a multiband radiofre-
²¹ quency pulse to simultaneously excite and receive signals from multiple slices, which can
²² also be leveraged to improve spatial resolution (Moeller et al., 2010; Feinberg and Setsom-
²³ pop, 2013). For a given period of acquisition time and voxel size, the number of volumes
²⁴ collected increases by the MB factor, e.g., an MB factor of eight increases the number of
²⁵ volumes eight-fold. This increase in the number of time points in itself can improve sta-
²⁶ tistical power (Todd et al., 2016). It can also improve the ability to unalias physiological
²⁷ sources of noise during temporal filtering (Todd et al., 2017) and improve artifact removal

28 using independent component analysis (Smith et al., 2013; Griffanti et al., 2017). However,
29 this increase in sampling frequency is accompanied by reduced signal-to-noise ratio from two
30 potential sources. First, noise amplification occurs during image reconstruction when indi-
31 vidual slices are recovered from the simultaneously excited overlapping slices. Coil geometry
32 factors (*g*-factors) are used to quantify this noise amplification and have been shown to vary
33 across the field of view. In general, *g*-factors tend to be highest in subcortical regions and,
34 in some studies, prefrontal areas where coil elements have lower and less variable sensitivity
35 (Risk et al., 2018; Todd et al., 2017). Second, the signal is attenuated by the shortened
36 repetition time (TR), which reduces equilibrium longitudinal magnetization even when the
37 Ernst angle is used for the excitation radiofrequency pulse.

38 For some cortical regions, such as the visual and motor cortex, the benefits of MB accel-
39 eration up to eight-fold appear to outweigh the costs, with improved detection of task-evoked
40 activity (Chen et al., 2015; Todd et al., 2017; Risk et al., 2018). Some benefits have also been
41 observed in resting-state networks in studies evaluating up to 4-fold acceleration (Demetriou
42 et al., 2018; Boyacioglu et al., 2015; Preibisch et al., 2015; Chen et al., 2020) and 6-fold ac-
43 celeration (Feinberg et al., 2010; Chen et al., 2015; Jahanian et al., 2019). However, previous
44 studies have not systematically evaluated how functional connectivity is related to *g*-factors,
45 nor the implications of this on subcortical regions in which *g*-factors are higher. Moreover,
46 the majority of the extant literature has only considered selected lower MB factors (sum-
47 marized in Bhandari et al. 2019) or considered a small number of subjects. A systematic
48 evaluation that includes the higher MB factors that are now common in large-scale rs-fMRI
49 studies is currently lacking.

50 The aim of this study is to characterize the impact of MB factor on correlation-based
51 functional connectivity in order to provide guidance for the design of rs-fMRI studies. Our
52 assessment uses standard preprocessing pipelines with nuisance regression (Fox et al., 2009)
53 with and without bandpass filtering. We evaluate MB factors ranging from 2 to 12 (2-mm
54 isotropic) and single-band (SB) acquisitions with two voxel sizes (2- and 3.3-mm isotropic)

55 in six-minute runs. We conduct our analyses at two levels: 1) an analysis of seed-based
 56 correlation maps for a seed in the right putamen and a seed in the hand region of left
 57 primary motor cortex (LM1); and 2) an examination of network connectivity using the 264-
 58 node atlas from [Power et al. \(2011\)](#), which includes thirteen subcortical nodes. We examine
 59 the putamen as it is in a high *g*-factor area, forms circuits with cortical regions critical
 60 for coordinating various aspects of behavior including movement ([Kravitz et al., 2010b](#)),
 61 memory ([Poldrack et al., 2001](#)), and motivation ([Pessiglione et al., 2006](#)), and has been
 62 implicated in both movement and cognitive disorders ([Kravitz et al., 2010a; Konova et al.,](#)
 63 [2013; Cerliani et al., 2015](#)). We examine LM1 because it is in a low *g*-factor area that allows
 64 an examination of spatial biases introduced by *g*-factor. It receives feedforward excitatory
 65 input critical for refining movements from the contralateral cerebellar dentate nucleus (also a
 66 low *g*-factor area), via the left ventrolateral thalamus ([Bastian and Thach, 1995; Dum and](#)
 67 [Strick, 2003](#)), which is in a high *g*-factor area.

68 2. Theoretical Background

69 2.1. Noise amplification and functional connectivity

70 Here we present a simplified model of the BOLD signal in which noise amplification
 71 reduces correlation. Let x_{ivt} represent the BOLD time series for the i th subject, v th lo-
 72 cation, and t th time point. For the moment, we assume that there is no multiband noise
 73 amplification. Let $x_{iv't}$ denote the time series for another location v' . Then

$$\begin{bmatrix} x_{ivt} \\ x_{iv't} \end{bmatrix} \sim \left(\begin{bmatrix} \mu_v \\ \mu_{v'} \end{bmatrix}, \begin{bmatrix} \sigma_v^2 & \psi_{vv'} \\ \psi_{vv'} & \sigma_{v'}^2 \end{bmatrix} \right). \quad (1)$$

74 Here, μ_v is the mean for the v th location and σ_v^2 its variance. The covariance between
 75 locations v and v' is $\psi_{vv'}$. The symbol \sim denotes “distributed as.” In the time series litera-
 76 ture, a constant mean and covariance matrix is referred to as “weakly stationary,” which we

77 specify without additional distributional or independence assumptions (Tsay, 2010). In par-
 78 ticular, the following model applies to any autocorrelation structure. The contemporaneous
 79 correlation between two locations v and v' is defined as

$$\text{Corr}(x_{ivt}, x_{iv't}) = \frac{\psi_{vv'}}{\sigma_v \sigma_{v'}} = \rho_{vv'}.$$

80 In SB functional connectivity studies that treat functional connectivity as constant across
 81 time, the contemporaneous correlation $\rho_{vv'}$ is the parameter of interest (e.g., Biswal et al.
 82 1995). We do not partition the sources of variance into neuronal, physiological, and thermal
 83 noise, as our purpose here is to present a model that conceptualizes the impact of multiband
 84 acceleration. Now let y_{iavt} denote the time series with MB factor equal to a . Then we define

$$y_{iavt} = x_{ivt} + \epsilon_{iavt}, \quad (2)$$

85 where ϵ_{iavt} is the noise due to multiband acceleration and is mean zero with variance η_{av}^2 .
 86 Then η_{av}^2 is the variance due to noise amplification for the a th MB factor and v th location.
 87 Additionally, we assume ϵ_{iavt} is independent of x_{ivt} . In the SB acquisition ($a = 1$), $\epsilon_{i1vt} = 0$ by
 88 definition. This model assumes that the covariance is constant across different acceleration
 89 factors. In practice, this assumption is likely violated due to signal attenuation in higher
 90 MB-factor experiments from shortened TR and therefore reduced equilibrium longitudinal
 91 magnetization. However, such reduction in longitudinal magnetization can be reformulated
 92 as a proportional increase in noise. Then,

$$\text{Corr}(y_{iavt}, y_{iav't}) = \frac{\psi_{vv'}}{\sqrt{\sigma_v^2 + \eta_{av}^2} \sqrt{\sigma_{v'}^2 + \eta_{av'}^2}}, \quad (3)$$

93 which results in lower correlations.

94 In this paper, we focus on two possible issues resulting from noise amplification: 1)
 95 spatial biases in functional connectivity estimates and 2) statistical power reduction. It is

96 well-known that g -factors vary spatially. Consequently, η_{av}^2 differs across v . In the model
 97 above, this results in spatially heterogeneous noise impacts on the BOLD time series, which
 98 lead to differences in functional connectivity between brain regions due to MB factor rather
 99 than neural activity.

100 With regard to statistical power, the trade-off between the costs and benefits of MB
 101 acquisition will be impacted by the extent to which the standard errors of the correlations
 102 are reduced by the increased number of time points in MB acquisitions. (We assume that
 103 the scan time is the same for different MB factors.)

104 Let $z_{avv'} = \text{arctanh}\{\text{Corr}(y_{iavt}, y_{iav't})\}$ be the Fisher z-transformed population corre-
 105 lation. To simplify the discussion, we examine a one-sided one-sample z-test for a true
 106 parameter $z_{avv'}$ with null hypothesis $H_0 : z_{avv'} \leq 0$ and alternative hypothesis $H_a : z_{avv'} > 0$.
 107 (The power function presented here is approximately equal to the power of a t-test for a
 108 large number of subjects.) We assume subject Fisher z-correlations have the same mean and
 109 variance: $\hat{z}_{iavv'} \stackrel{iid}{\sim} \mathcal{N}(z_{avv'}, \nu_{avv'}^2)$ for all $i = 1, \dots, N$, where the symbol $\stackrel{iid}{\sim}$ denotes “inde-
 110 pendently and identically distributed,” $\mathcal{N}(z_{avv'}, \nu_{avv'}^2)$ is the normal distribution with mean
 111 $z_{avv'}$ and variance $\nu_{avv'}^2$, and N is the number of subjects. The BOLD time series generating
 112 the correlations are known to contain autocorrelation (i.e., $\text{Corr}(y_{iavt}, y_{iav(t-l)}) \neq 0$ for some
 113 lag l), but this does not affect the validity of the assumption that subjects are independent,
 114 as discussed in Section [2.2 Autocorrelation and other considerations for multiband data](#). Let
 115 $c_{1-\alpha} = \Phi^{-1}(1 - \alpha)$ be the critical value for a level- α test, where $\Phi(\cdot)$ is the standard normal
 116 cumulative distribution function (CDF) and $\Phi(\cdot)^{-1}$ the inverse CDF. Then the power is

$$\Phi\left(\sqrt{N} \frac{z_{avv'}}{\nu_{avv'}} - c_{1-\alpha}\right). \quad (4)$$

117 Note that in this model, an increase in the MB factor may simultaneously *decrease* $z_{avv'}$,
 118 since the noise amplification decreases the correlation via (3), and *decrease* $\nu_{avv'}$, since the
 119 higher number of volumes may decrease the standard deviation of the sample correlation

120 (discussed in Section [2.2 Autocorrelation and other considerations for multiband data](#)). Thus,
121 the benefit of MB on functional connectivity estimation depends on the balance between the
122 cost of noise amplification at the locations of interest and the increase in the number of
123 volumes acquired.

124 Although we have presented (4) for a one-sample test, a similar argument applies to
125 the more common scenario in which correlations are being compared between groups, e.g.,
126 healthy and diseased, as described in [Appendix A Power when comparing two groups](#).

127 *2.2. Autocorrelation and other considerations for multiband data*

128 The autocorrelation in multiband data does not affect the validity of the group test
129 statistics in the sense that when the null hypothesis is true, the type-1 error rate is approx-
130 imately equal to the specified α -level. However, the power is impacted by autocorrelation
131 via the impact on the variance of $\hat{z}_{iavv'}$, denoted $\nu_{avv'}^2$. In the absence of autocorrelation
132 (i.e., white noise), $\nu_{avv'}^2 \approx 1/T_a$, where T_a is the number of time points in acquisition a .
133 For N independent subjects, $\text{Var} \sum_{i=1}^N \hat{z}_{iavv'} / N \approx 1/(NT_a)$. In general, $\nu_{avv'}^2 > 1/T_a$ in the
134 presence of positive autocorrelation. Intuitively, for a fixed scan time with increasing MB
135 factor a , the benefits of a larger T_a decline as the autocorrelation increases due to a decrease
136 in the effective degrees of freedom. We present an additional discussion of the implications
137 of autocorrelation in [Appendix B Implications of autocorrelation on power](#).

138 Another complication of MB acquisitions is that correlations may exist between aliased
139 voxels. Voxels collected in the same multiband group are aliased according to the blipped-
140 CAIPI (Controlled Aliasing In Parallel Imaging) field-of-view (FOV) shifts, as illustrated
141 in [Todd et al. \(2016\)](#). In simulations with slice-GRAPPA reconstruction (no leak block),
142 [Setsompop et al. \(2013\)](#) found that MB acquisitions can result in artifactual thermal noise
143 correlations if v and v' are aliased. Using the model in (2), this implies $\text{Cov}(\epsilon_{iavt}, \epsilon_{iav't}) \neq 0$ if
144 v and v' are aliased. Previous studies with task fMRI indicate that the split slice-GRAPPA
145 algorithm, as now used in Siemens reconstruction (leak block), dramatically reduces aliasing
146 artifacts ([Cauley et al., 2014](#); [Todd et al., 2016](#); [Risk et al., 2018](#)). In the simplified model in

¹⁴⁷ Section [2.1 Noise amplification and functional connectivity](#), we assume the possible increase
¹⁴⁸ in correlations between aliased voxels is negligible. This is discussed more in Section [5.4](#)
¹⁴⁹ [Preprocessing pipelines and strategies for artifact and noise removal](#).

¹⁵⁰ **3. Methods**

¹⁵¹ *3.1. Participants and imaging protocol*

¹⁵² Thirty-two (16 female, ages 19-29) healthy, unmedicated, right-handed young adults par-
¹⁵³ ticipated in this study, who were recruited from Emory University and the surrounding
¹⁵⁴ community. Nine six-minute resting-state fMRI runs were acquired from each participant on
¹⁵⁵ a 3T MR scanner using a 32-channel head coil padded with foam wedges to decrease head mo-
¹⁵⁶ tion. Each participant's data is from a single session in the same scanner, and two scanners
¹⁵⁷ with identical hardware specifications and software version were used throughout the study
¹⁵⁸ (MAGNETOM PrismaFit, software version E11C, Siemens Healthcare, Erlangen, Germany).
¹⁵⁹ Multiband scans were collected using 2D multiband echo-planar imaging (EPI) sequences
¹⁶⁰ with blipped-CAIPI, Development Release R016a, from the Center for Magnetic Resonance
¹⁶¹ Research (CMRR), University of Minnesota ([Moeller et al., 2010](#); [Setsompop et al., 2012](#);
¹⁶² [Xu et al., 2013](#)). Details on the nine resting-state fMRI acquisitions are in Table 1, with
¹⁶³ flip angles set to achieve the Ernst angle. Echo time (TE)=32 ms in all acquisitions except
¹⁶⁴ MB 12, where TE=32.4. Parameters common to multiband scans include $2 \times 2 \times 2 \text{ mm}^3$
¹⁶⁵ voxels, $208 \times 208 \text{ mm}^2$ in-plane field of view, 72 slices, 0 mm slice gap, integrated paral-
¹⁶⁶ lel imaging technique (iPat)=none, phase partial Fourier=7/8, anterior-to-posterior (AP)
¹⁶⁷ phase encoding direction, interleaved slices, pre-scan normalize, and scanner reconstruction
¹⁶⁸ using the LeakBlock option, i.e., split slice-GRAPPA (GeneRalized Autocalibrating Partial
¹⁶⁹ Parallel Acquisition) ([Cauley et al., 2014](#)), and sum-of-squares coil combination. The MB
¹⁷⁰ factors correspond to all possible factors with 72 slices available in the CMRR sequences,
¹⁷¹ which corresponds to all integers a less than or equal to 12 such that $72/a$ is a whole num-
¹⁷² ber. An SB reference acquisition with AP encoding (SBRef AP) was acquired prior to each

MB	1	1	2	3	4	6	8	9	12
TR (ms)	3000	5670	2850	1910	1440	962	736	675	512
Voxel Size	3.3	2	2	2	2	2	2	2	2
Flip Angle	81	88	80	72	65	57	51	48	43
Number of volumes	114	62	121	182	241	353	464	505	668
DF lost in bandpass	65	13	72	133	192	306	415	458	619
DF after 9p+bandpass	37	37	37	37	37	35	37	35	37

Table 1: Resting-state fMRI acquisitions. Voxels are isotropic. All runs were approximately six minutes. Volumes corresponding to the first 10 seconds were removed. Degrees of freedom (DF) after 9p+bandpass is equal to the number of volumes minus 3 (constant, linear, quadratic) minus 9 (6 parameters from rigid-body, global signal, white matter, and cerebrospinal fluid) minus the number of frequencies used in the discrete cosine basis in the time-domain bandpass filtering via AFNI’s 3dTproject.

173 MB acquisition, which is required for multiband image reconstruction. An additional SB
 174 reference acquisition with posterior-to-anterior encoding (SBRef PA) was acquired prior to
 175 the MB 3 acquisition for use in distortion correction, as described in Section [3.2 FMRI data](#)
 176 [processing](#). The order of the MB factors was randomized for each subject. Participants
 177 were asked to lay motionless and look at a cross-hair during resting-state scans. A T1-
 178 weighted magnetization-prepared rapid gradient-echo (MPRAGE) sequence (TR/Inversion
 179 Time (TI)/TE = 2300/900/3.02 ms, flip angle = 8 degrees, field of view = $256 \times 256 \text{ mm}^2$,
 180 $1 \times 1 \times 1 \text{ mm}^3$ voxels, 176 slices) was collected after the first five resting-state acquisitions.
 181 A landscapes movie was played during the MPRAGE acquisition. This study was approved
 182 by the Institutional Review Board of Emory University and participants provided written
 183 informed consent.

184 [3.2. FMRI data processing](#)

185 [Motion correction](#). Volumes corresponding to the first 10 seconds of the run were removed
 186 for each acquisition. Then the seven MB acquisitions (MB 2, MB 3, MB 4, MB 6, MB 8,
 187 MB 9, MB 12) were motion-corrected to their corresponding SB reference AP images using
 188 rigid body alignment (6 DOF) in MCFLIRT ([Jenkinson et al., 2002](#)) in FSL 6.0.3. SB 2 mm
 189 and SB 3.3 mm were registered to the eighth volume of their scans.

190 [Susceptibility distortion correction](#). The SBRef PA acquisition was rigid body aligned to
 191 the SBRef AP MB 3. Then FSL’s topup was applied ([Andersson et al., 2003; Smith et al.,](#)

192 2004). The 2 mm resting-state acquisitions were then aligned to the SBRef AP MB 3 using
193 a rigid body transformation, topup applied, followed by slice-timing correction. The 3.3
194 mm acquisition was slice-timing corrected, spline-interpolated to $2 \times 2 \times 2$ mm³ resolution,
195 followed by topup.

196 Co-registration and normalization to MNI. Distortion and motion-corrected resting-state
197 acquisitions were then rigid-body aligned to the anatomical image. The anatomical im-
198 age was non-linearly registered to the Montreal Neurological Institute 152 template in FSL
199 (MNI152_T1_2mm) using FNIRT, and the warping function was then applied to the resting-
200 state acquisitions. Acquisitions were then skull stripped and intensity normalized to result
201 in the global (4d) mean equal to 10,000 (Glasser et al., 2013).

202 Nuisance regression, temporal filtering, and spatial smoothing. We further processed the
203 data to minimize BOLD variance unlikely to represent neural activity in preparation for func-
204 tional connectivity analyses using the “9p” nuisance regression model in Ceric et al. (2017).
205 The nine nuisance regressors in this model are the six rigid body realignment parameters,
206 global signal, average cerebrospinal fluid (CSF) signal, and average white matter (WM) sig-
207 nal. We chose this model because global signal regression (GSR) is particularly effective
208 at removing head motion and respiratory-related artifacts from functional connectivity esti-
209 mates (Power et al., 2017, 2019, 2020), and the 9p pipeline maximized a measure of network
210 quality in Ceric et al. (2017), suggesting a balance between reducing artifacts and preserving
211 signal. We chose a pipeline commonly found in the literature, rather than a more special-
212 ized pipeline, to improve the generalizability of our results. In addition, we implemented
213 three variations of the 9p pipeline to investigate the impacts of temporal filtering and spa-
214 tial smoothing: 1) 9p with bandpass filtering applied during nuisance regression, hereafter
215 denoted as 9p+bandpass; 2) 9p with 6-mm full width at half maximum (FWHM) spatial
216 smoothing, hereafter 9p+spatial smoothing; and 3) 9p+bandpass+spatial smoothing. We
217 used the FSL tissue priors for WM and CSF, where a binary mask was created by setting
218 voxels equal to one if their probability was greater than > 0.5 and zero otherwise. Nuisance

regression, bandpass filtering, and spatial smoothing were implemented using AFNI 19.3.16 (Cox, 1996). We used AFNI’s 3dTproject to bandpass from 0.009 to 0.08 Hz, in which a single design matrix is created from the nuisance regressors and cosine and sine functions (at the frequencies 0 to 0.009 and 0.08 and higher). This simultaneously performs bandpass filtering and nuisance removal, as recommended in Hallquist et al. (2013), Lindquist et al. (2019), and Bright et al. (2017), and the residuals from least squares are retained for subsequent correlation analyses. In Table 1, we indicate the number of regressors included in the nuisance regression, where “DF lost in bandpass” indicates the number of covariates included in the design matrix to achieve bandpass filtering.

In line with recent recommendations (Ciric et al., 2017), we excluded scans with excessive gross motion defined as scans with mean relative root mean squared displacement exceeding 0.2 mm or 1/6th of scans exceeding 0.25 mm relative root mean squared displacement, resulting in the exclusion of nine scans. Additionally, MB 9 scans were not collected in the first two subjects. Thus, there were 277 scans used in subsequent analyses (31 SB 3.3 mm, 31 SB 2 mm, 30 MB 2, 29 MB 3, 31 MB 4, 32 MB 6, 32 MB 8, 29 MB 9, 32 MB 12).

3.3. Noise amplification

For each scan and processing pipeline, we calculated the standard deviation of the time series on a voxel-wise basis, creating a standard deviation map for each scan. Let \hat{s}_{iav} denote the sample standard deviation for the v th voxel and a th acceleration factor in the i th subject, calculated across the T_a time points. Recall the definitions of σ_v^2 and η_{av}^2 from equations (1) and (2) in Section 2.1 *Noise amplification and functional connectivity*. Then $E \hat{s}_{iav}^2 = \sigma_v^2 + \eta_{av}^2$, where E denotes the expectation. For each pipeline, we calculated $\bar{s}_{av} = \sum_i \hat{s}_{iav}/N$, resulting in the average standard deviation maps. We visually assessed how bandpass filtering impacted the variance due to noise amplification, and also the variance due to physiological sources (CSF and cardiac) that still remained after nuisance regression.

The g -factors provide insight into which brain regions may be adversely impacted by noise amplification resulting from multiband acquisition and reconstruction. In the absence

246 of acceleration, thermal noise is white noise that is spatially and temporally homogeneous
247 and independent of the signal (Chen et al., 2019). With no in-plane acceleration, the noise
248 amplification of the thermal noise component can be described by defining the *g*-factor as
249 $g = SNR_{full}/SNR_{acc}$, where SNR_{full} is the signal-to-noise ratio in the single-band data and
250 SNR_{acc} is the SNR in the accelerated multiband data (Breuer et al., 2009). In this study,
251 we do not use in-plane acceleration in rs-fMRI acquisitions.

252 Since we obtained SB and MB images from every subject, we generated apparent *g*-
253 factor maps in the processed data as the ratio of the standard deviation across time in
254 the accelerated acquisitions to the standard deviation in the SB 2 mm acquisition for each
255 subject. Let \hat{s}_{i1v} denote the standard deviation for the *i*th subject in the SB 2-mm acquisition
256 at the *v*th location. The apparent *g*-factor is defined

$$g_{iav} = \hat{s}_{iav}/\hat{s}_{i1v}. \quad (5)$$

257 This definition is similar to that used in Preibisch et al. (2015), except that we use the ratio
258 of standard deviations in preprocessed data rather than SNR from minimally preprocessed
259 data. Recall the mean of the data are scaled to equal 10,000 prior to nuisance regression,
260 which ensures the standard deviations are on comparable scales. Also note the nuisance
261 regression removes the mean, so a ratio of SNRs is not possible. The nuisance regression
262 decreases the standard deviation by reducing physiological and motion effects. If the shorter
263 TR in multiband facilitates the removal of nuisance variance, then this measure accounts
264 for this benefit. It is noteworthy that this ratio combines the effects of reconstruction noise,
265 physiological noise, and reduced signal due to reduced longitudinal magnetization resulting
266 from the shortened TR.

267 In addition, we partitioned the brain into 247 cortical, 13 subcortical, and four cerebellar
268 regions of interest (ROIs) defined using 5-mm radius spheres centered at the MNI coordinates
269 in Power et al. (2011), and calculated the apparent *g*-factors for each of the 264 nodes. These

270 g -factors were then visualized using the BrainNet viewer 1.7 (Xia et al., 2013).

271 *3.4. Impacts on seed map correlations*

272 We examined the impact of acquisition on connectivity for two seed regions: 1) a 4-mm
273 radius sphere in the dorsal rostral putamen centered at MNI (25, 8, 6), which is in a high
274 g -factor area and was found to have hyperconnectivity in children with ASD (Di Martino
275 et al., 2011), and 2) a 5-mm radius sphere centered at MNI (-41, -20, 62), which is in a low
276 g -factor area, was identified as the peak task-related activation localized to the precentral
277 gyrus during a right-hand finger sequencing task in Buckner et al. (2011), and is connected
278 to other motor regions in both low and high g -factor areas.

279 For each seed, scan, and processing pipeline, time series for voxels within the seed region
280 were averaged, and a seed correlation map generated by calculating the correlation between
281 the seed time course and every other voxel in the brain. We visualized maps for each seed
282 by averaging these correlations across subjects for each acquisition and pipeline. We also
283 compared connectivity effect sizes for each seed by Fisher z-transforming the correlations
284 and then calculating Cohen's d. For a given correlation, the Cohen's d statistic characterizes
285 the effect size against the null hypothesis that the group correlation is equal to zero. Our
286 primary analysis used the 9p and 9p+bandpass pipelines, allowing the possibility of higher
287 resolution seed maps for the 2 mm acquisitions. Results with smoothing are presented in
288 the Web Supplement.

289 *3.5. Impacts on pairwise correlations in a functional atlas*

290 *3.5.1. Impacts on the magnitude of correlations*

291 To calculate functional connectivity between pairs of brain regions, we again used the set
292 of 264 5-mm radius spheres centered at the MNI coordinates in Power et al. (2011). This
293 commonly used atlas is based on functional areas and classifies ROIs (nodes) into thirteen
294 functional communities, with some nodes labeled in a fourteenth category as "uncertain."
295 An advantage of this parcellation is that all nodes are the same size; parcellations with

296 regions of different size result in an additional source of heteroscedasticity unrelated to noise
 297 amplification, where larger regions tend to have reduced variance. Using Matlab R2020a,
 298 time series for voxels within each 5-mm sphere were averaged; correlations between average
 299 ROI time series were calculated and Fisher z-transformed.

300 To understand the impact of MB factor on pairwise correlations, we propose a measure
 301 that combines the effects of the standard deviations at each node (ROI) in an edge:

$$g*i_{avv'} = \frac{\hat{s}_{iav}\hat{s}_{iav'}}{\hat{s}_{i1v}\hat{s}_{i1v'}} = g_{iav}g_{iav'}, \quad (6)$$

302 where g_{iav} is defined in (5). We define two different sets of $g*$ -factors to correspond to the
 303 standard deviations from the 9p and 9p+bandpass pipelines. To visualize the impact of $g*$ -
 304 factors on edge correlations, we averaged Fisher z-transformed correlations across subjects
 305 for each edge, i.e., $\sum_i \hat{z}_{iavv'}/N$, and then plotted the MB correlations versus the SB 2 mm
 306 correlations for each edge colored by $\sum_i g *_{iavv'}/N$.

307 Next, we visualized plots of correlation matrices for the 9p and 9p+bandpass pipelines
 308 to see where the impacts occurred. We excluded the “uncertain” category from visual sum-
 309maries of the correlation matrices. Plots from 9p+spatial smoothing and 9p+bandpass+spatial
 310 smoothing were similar and are not displayed.

311 To statistically examine the impacts on power, we subset to select intra-community edges
 312 where we expect positive correlations (i.e., edges between nodes within the same functional
 313 community) and which represented a range of $g*$ -factors. Specifically, we used an edge
 314 between the left and right thalamus (ROIs 224 and 225), left and right putamen (227 and
 315 230), left and right cerebellum (244 and 245), six edges from nodes in executive control
 316 (192, 195, 196, 201), salience (212, 217, 218, 220), and default mode (88, 92, 109, 110). The
 317 cortical nodes were selected based on their proximity to the regions in [Chand et al. \(2017\)](#).

318 Using this subset, we created a generalized additive mixed model (GAMM) (Gaus-
 319 sian family) with the Fisher z-transformed correlations ($\hat{z}_{iavv'}$) as the response variable, a

smoother for g^* -factor ($g^*_{iavv'}$) with smoothing selected using restricted maximum likelihood (REML), fixed effects of edge, gender, and scanner, a random effect for participant, and a random effect for the interaction between participant and edge using the package mgcv 1.8-33 (Wood, 2017) in R 3.6.0. The use of the GAMM allows for a possible non-linear relationship between the Fisher z-transformed correlations and g^* -factor. Note this analysis pools across the MB factors, where the MB factor drives the variation in g^* -factors, with repeated measurements accounted for via the random effects. Also note that we did not conduct a parallel analysis with 9p+bandpass because the bandpass filtering results in g^* -factors close to one, as will be seen in Section 4.3 Impacts on pairwise correlations in a functional atlas.

We used generalized estimating equations with robust standard errors (Gaussian family) implemented in the R package geepack 1.3-1 (Halekoh et al., 2006) to examine the impact of MB factor on correlations for the subset of intra-community edges described above. We conducted this analysis for the 9p, 9p+bandpass, 9p+spatial smoothing, and 9p+bandpass+spatial smoothing. We created separate models for the thalamus, putamen, cerebellum, executive control, salience, and default mode. The Fisher z-transformed correlation ($\hat{z}_{iavv'}$) was the response variable with MB factor, gender, and scanner as categorical variables and participant id as the clustering variable. The SB 2 mm acquisition was used as the reference level for MB factor.

3.5.2. Impacts on edge density

We examined edge density for each of the thirteen communities. For each pipeline, we conducted one-sample t-tests for each edge to test that the population correlation was equal to zero using the sample z-transformed correlations from each subject. There were a few spheres in the “uncertain” category (ROIs 4, 5, 9, 10, and 250) and one in default mode (ROI 83) that contained no data in some subjects in the SB 3.3 mm distortion-corrected image. We excluded these six nodes. We calculated the proportion of significant edges for each of the communities in Power et al. (2011) using the Bonferroni-level $\alpha = 0.05/(258 * 257/2)$, which suffices here since the effect sizes are large. The proportions were calculated using all

³⁴⁷ possible edges (i.e., inter- and intra-community). Since the number of subjects for each MB
³⁴⁸ factor varied from 29 to 32, we standardized the power across MB factor by calculating the
³⁴⁹ t-statistics as the Cohen's d multiplied by $\sqrt{32}$ (the most common number of subjects) and
³⁵⁰ used a t-distribution with $df = 31$ for all MB. Thus differences in the proportion of activated
³⁵¹ voxels are primarily attributable to MB factor rather than sample size.

³⁵² We assessed whether the differences between the proportion of significant correlations
³⁵³ were meaningful by conducting permutation tests using MB 8 as a reference as follows: 1)
³⁵⁴ we subset to subjects that passed the quality control criteria in both the given acquisition
³⁵⁵ and MB 8; 2) permuted the MB factor to create pseudo acquisition groups; 3) for each
³⁵⁶ pseudo group and for each edge, calculated one-sample t-tests; 4) for each pseudo group
³⁵⁷ and each community, calculated the proportion of edges with significant correlations at $\alpha =$
³⁵⁸ $0.05/(258*257/2)$ (including all edges in which at least one node belonged to the community);
³⁵⁹ and 5) for each community, calculated the absolute value of the difference between the
³⁶⁰ proportion significant in pseudo group 1 and the proportion significant in pseudo group
³⁶¹ 2. These steps were repeated 10,000 times, and we then calculated the fraction of absolute
³⁶² differences from the pseudo groups that were greater than the absolute difference when using
³⁶³ the true MB factor labels, thereby generating two-sided (uncorrected) p-values. Our primary
³⁶⁴ analysis focused on the 9p and 9p+bandpass pipelines, with additional results for 9p+spatial
³⁶⁵ smoothing in the Web Supplement. We also conducted permutation tests using the same
³⁶⁶ steps to compare the proportion of significant correlations in 9p versus 9p+bandpass for each
³⁶⁷ multiband factor. These tests were implemented using our own scripts in R 3.6.0.

³⁶⁸ *3.6. Impacts in independent datasets*

³⁶⁹ *3.6.1. Evaluation of a third scanner using a 64-channel head coil*

³⁷⁰ We examined whether our findings were similar in a dataset with three additional subjects
³⁷¹ (all 27 years old, 1 female) collected using a 64-channel head and neck coil at the Center
³⁷² for Advanced Brain Imaging and Neurophysiology, University of Rochester, NY, USA. The
³⁷³ same acquisition and preprocessing was applied to these subjects. In this cohort, the mean

³⁷⁴ relative root mean squared displacement was < 0.2 mm in all acquisitions. There were four
³⁷⁵ acquisitions in which > 1/6 of volumes had > 0.25 mm framewise displacement (subject 1:
³⁷⁶ SB 2 mm and MB 2; subject 3: MB 4 and MB 6). Unlike the primary cohort, all acquisitions
³⁷⁷ were used in subsequent analyses because we only had three subjects.

³⁷⁸ We created standard deviation maps averaged across the three subjects, as in [3.3 Noise
379 amplification](#), for 9p and 9p+bandpass.

³⁸⁰ We created seed maps for the dorsal rostral putamen described in Section [3.4 Impacts
381 on seed map correlations](#) for the four pipelines (9p, 9p+bandpass, 9p+spatial smoothing,
382 9p+bandpass+spatial smoothing).

³⁸³ We calculated Fisher z-transformed correlations as described in Section [3.5.1 Impacts
384 on the magnitude of correlations](#) and compared the correlation matrices across multiband
385 factors.

³⁸⁶ *3.6.2. Evaluation of pairwise correlations in the preprocessed Young Adult Human Connec-
387 tome Project data*

³⁸⁸ To gain insight into the generalizability of spatial differences in correlations and effect
389 sizes to other pipelines and datasets, we estimated correlation matrices from the ICA-FIX
390 preprocessed rs-fMRI data in the Young Adult Human Connectome Project, which used MB
391 8 ([Smith et al., 2013](#)). This analysis is presented in Web Supplement [S.4.2 Evaluation of
392 pairwise correlations in the preprocessed Young Adult Human Connectome Project data](#).

³⁹³ **4. Results**

³⁹⁴ *4.1. Noise amplification*

³⁹⁵ The impact of multiband acceleration on noise amplification is clearly visible from the
396 voxel-wise standard deviations of the resting-state time series (Figure 1). There is a shift
397 from a physiologically dominated noise regime in SB acquisitions, in which there are large
398 contributions to the BOLD signal from CSF pulsation in the third ventricle, cerebral aque-
399 duct, fourth ventricle, and central canal, and the sagittal sinus is also apparent (prominent

400 in MB 3 in first column), to a reconstruction-noise dominated regime (standard deviations
401 greater than 300 across interior regions in MB 8 and higher, column A of Figure 1). Although
402 CSF nuisance regression reduced physiological noise variance, CSF pulsation still appears to
403 be prominent in some regions. There may also be variance due to intracranial brain motion
404 during the cardiac cycle. Examining column B, it is clear that the bandpass filtering reduces
405 physiological sources of variance in the acquisitions with higher sampling rates, as the CSF
406 contributions in MB 4 to MB 12 are much less prominent relative to SB 3.3 mm, SB 2 mm,
407 MB 2, and MB 3. Adjusting the color gradient to increase the contrast in the 9p+bandpass
408 maps, in column D we see that there are still sources of physiological variance at the high
409 sampling rates, but it is reduced relative to slower acquisitions. Overall, the variance of MB
410 4 and greater is reduced relative to SB, MB 2, and MB 3. In the SD maps for the 9p+spatial
411 smoothing and 9p+bandpass+spatial smoothing, the standard deviation is greatly reduced
412 relative to unsmoothed data, as expected. The noise amplification increases with MB fac-
413 tor in the 9p+smooth pipeline, and physiological noise variance is reduced with bandpass
414 filtering at higher MB factors, similar to the unsmoothed data (Web Supplement Figure S.3).

415 Examining g -factor by node revealed patterns largely consistent with those observed in
416 the standard deviation maps. For the 9p processed data, g -factors are smallest for MB 2
417 (close to one) with increases in subcortical areas, as well as some nodes in the insula and
418 medial areas (Web Supplement Figures S.1 and S.2). In subcortical nodes, g -factors were
419 near 1.5 in MB 4, 2.25 in MB 8, and 3 in MB 12 (see Web Supplement File 1 containing
420 g -factors for each node), moderate noise amplification in the cerebellum (approximately
421 1.3 in MB 4, 1.6 in MB 8, and 2.4 in MB 12), low noise amplification in somatomotor
422 regions (approximately 1.2, 1.3, and 1.6 for MB 4, 8, and 12), and low in visual regions
423 (approximately 1.3, 1.4, and 1.6 for MB 4, 8, and 12). For 9p+bandpass data, g -factors are
424 close to one even in subcortical regions (approximately 1.0 in MB 4, 1.1 in MB 8, and 1.2 in
425 MB 12), and tend to be less than 1 in cortical regions, indicating decreased variation relative
426 to the SB 2 mm (e.g., MB 8 in the right column in Web Supplement Figure S.2 is in general

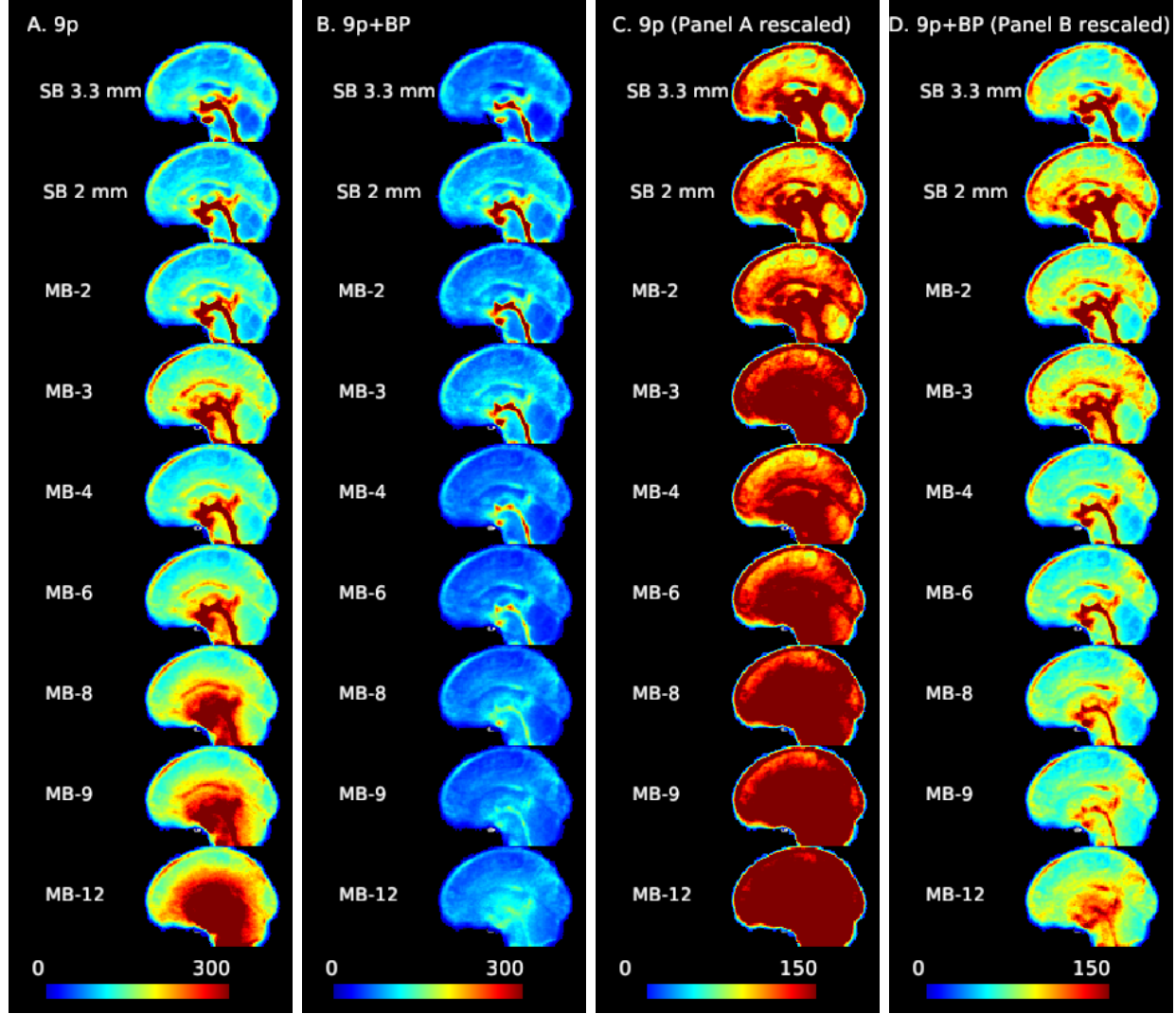


Figure 1: Noise amplification due to multiband acceleration and impacts of bandpass filtering. The standard deviation of the time series for each voxel (averaged across subjects) with 9p preprocessing (columns A and C) and 9p+bandpass (columns B and D). Sagittal slice with cursor at MNI=0. At higher MB factors, variance from noise amplification becomes more prominent. Columns A and B use a scale from 0 to 300, and columns C and D are the same data but using a scale from 0 to 150. As the MB factor increases, there is a shift from the physiologically dominated noise regime (in which the CSF pulsation is visible in the central canal, third ventricle, cerebral aqueduct, and fourth ventricle, with possible contributions from the superior and inferior sagittal sinus) to physiological plus noise amplification. The bandpass filtering reduces the overall variance and physiological contributions of CSF, veins, and arteries. In the rescaled version (column D), some ventricles, veins, and arteries are still visible at higher MB factors but less prominent.

⁴²⁷ more blue than MB 2 in the right column in Web Supplement Figure S.1). This is consistent
⁴²⁸ with Figure 1, in which the higher MB factors have smaller standard deviations.

⁴²⁹ *4.2. Impacts on seed map correlations*

⁴³⁰ Figure 2 illustrates correlation and effect size maps for the dorsal rostral putamen seed.
⁴³¹ For the 9p pipeline (column A), robust functional connectivity is observed with the left
⁴³² putamen as well as with the insula (fuchsia arrow) and bilateral thalamus (green arrow) in
⁴³³ the SB 3.3 mm data. Weak correlations with the cingulate cortex (anterior and medial to
⁴³⁴ the putamen, red arrow) are also visible. For SB 2 mm, MB 2, and MB 4, correlations with
⁴³⁵ the left putamen and bilateral insula are visible but weaker than SB 3.3 mm, whereas these
⁴³⁶ correlations are very small in MB 8 and higher. For the 9p+bandpass pipeline (column B),
⁴³⁷ the correlations are generally higher, resulting in clear delineation of the left putamen in MB
⁴³⁸ 2 to MB 8, although correlations with the cingulate are still not visible. Correlations in the
⁴³⁹ insula and thalamus are stronger in SB 3.3 mm, MB 2, and MB 4 than in other acquisitions.
⁴⁴⁰ In the left insula, there is a suggestion of better spatial specificity in MB 2 and MB 4 versus
⁴⁴¹ SB 3.3 mm, where the higher resolution may result in an improvement in the boundary
⁴⁴² between the left putamen and insula.

⁴⁴³ Comparing the rows in column C of Figure 2, the effect sizes within the putamen are
⁴⁴⁴ notably higher in SB 3.3 mm compared to the other acquisitions. Among the 2 mm ac-
⁴⁴⁵ quisitions, contralateral effects are more apparent in MB 4, MB 2, and MB 6 than others.
⁴⁴⁶ Contralateral effects decline at MB 8 and higher, and are also relatively poor in SB 2 mm.
⁴⁴⁷ Putamen-cortical and putamen-thalamic connectivity also appear higher in SB 3.3 mm com-
⁴⁴⁸ pared to the 2 mm acquisitions. Areas of the cingulate cortex are visible in SB 3.3 mm
⁴⁴⁹ in 9p (see red arrow in column A) but are reduced in 9p+bandpass (column D); this area
⁴⁵⁰ has Cohen's $d < 0.4$ in the MB and SB 2 mm acquisitions (columns C and D). In spatially
⁴⁵¹ smoothed data, the effect sizes were also largest in SB 3.3 mm (Web Supplement Figures
⁴⁵² S.4 and S.5). Effect sizes were overall much higher in spatially smoothed data, but at the
⁴⁵³ cost of a decrease in spatial specificity, and large effect sizes extended across anatomical

454 boundaries. In particular, the putamen and thalamus appear as a single structure (Web
455 Supplement Figure S.4). The differences in effect sizes between SB 3.3 mm and the MB
456 acquisitions are clearly illustrated in Web Supplement Figure S.5. In summary, SB 3.3 mm
457 most clearly reveals both cortical and subcortical functional connectivity with the putamen.

458 Figure 3 illustrates correlation and effect size maps for the LM1 seed. The correlations
459 between the motor cortex and the thalamus (green arrow) are clearly visible in the SB
460 3.3 mm acquisition for both 9p and 9p+bandpass (columns A and B, respectively), but
461 less apparent in the MB acquisitions. The left motor cortex is an area with low *g*-factor
462 (approximately 1.15, 1.25, and 1.7 for MB 4, MB 8, and MB 12, respectively), while the
463 thalamus is an area with high *g*-factor (approximately 1.25, 3.25, and 4.75 for MB 4, MB 8,
464 and MB 12). Thalamocortical correlations are very small in the MB acquisitions with 9p,
465 and are still weak in most MB acquisitions in 9p+bandpass, with MB 2 and MB 4 showing
466 stronger correlations than higher MB factors. In the thresholded Cohen's d maps, the 9p
467 and 9p+bandpass (columns C and D, respectively) show similar results overall. Again,
468 thalamocortical connectivity is clearly apparent in the SB 3.3 mm acquisition, with smaller
469 but notable effect sizes in the MB 2 to MB 6 acquisitions. In contrast, connectivity with
470 right M1, which is in a low *g*-factor area, is strong across all acquisitions. In addition, seed
471 and Cohen's D maps in Figure 3 nicely trace portions of the insular cortex, with larger effect
472 sizes in SB 3.3 mm.

473 We also examined the correlations between the left motor cortex and a region in right
474 lobule V of the cerebellum with low-to-moderate *g* factor (approximately 1.5, 2.2, and 3.7
475 for MB 4, MB 8, and MB 12). The cerebellum is structurally connected to the motor cortex
476 via both efferent and afferent pathways through the ventrolateral thalamus and the pontine
477 nucleus, respectively; consequently, some degree of functional connectivity is expected. For
478 example, Buckner et al. (2011) observed correlations of roughly 0.08 between the left motor
479 cortex and the right lobule V using SB data collected from 1000 participants, and these
480 correlations were notably higher than in neighboring locations within the cerebellum. In

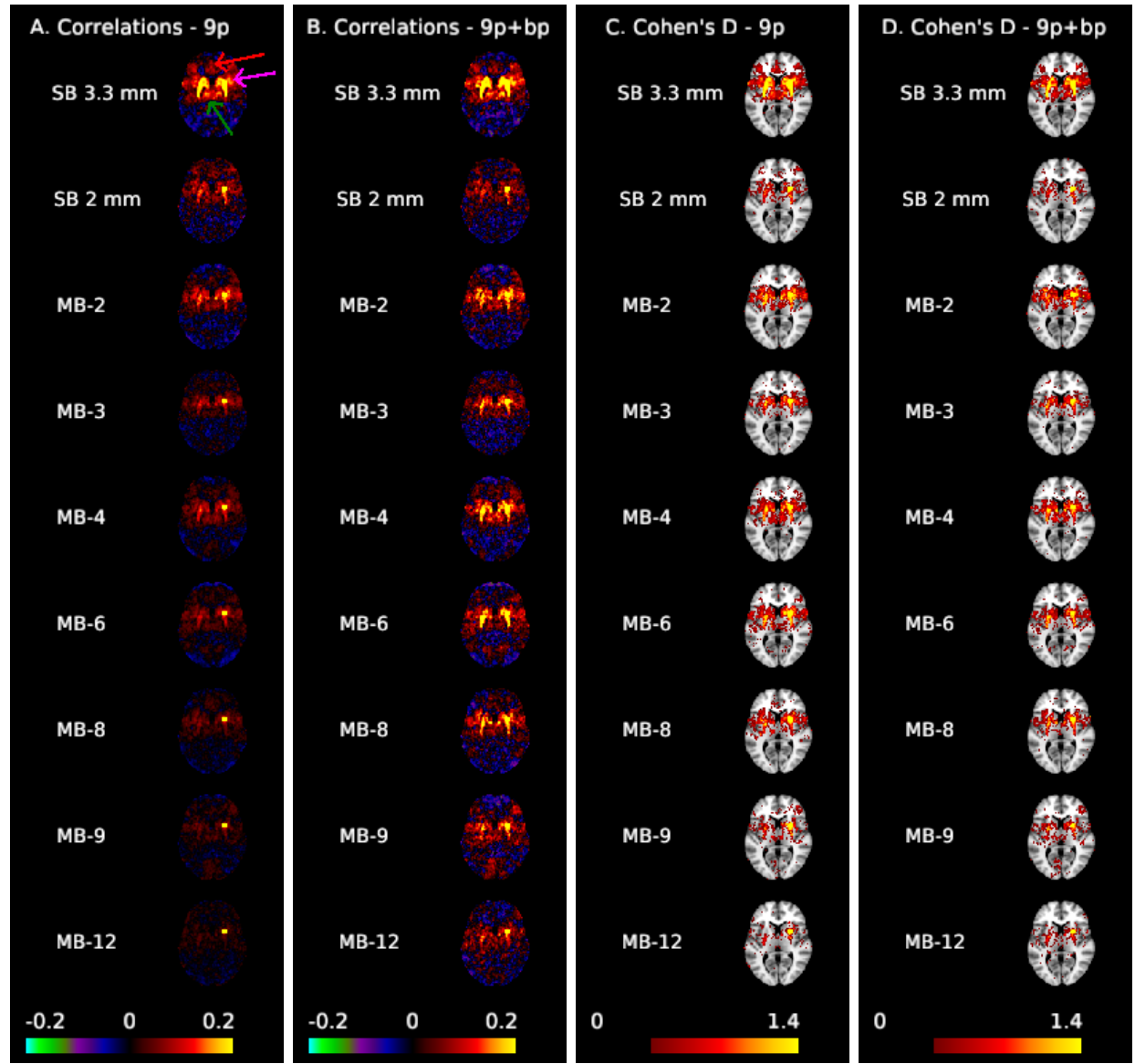


Figure 2: Correlation (A,B) and Cohen's d maps thresholded to display values >0.4 (C,D) for the dorsal rostral putamen seed (MNI: 25, 8, 6) shown at MNI axial slice 6. The arrows in column A highlight the cingulate cortex (red), insula (fuchsia), and thalamus (green). Spatial biases in the correlations increase as MB factor increases; ipsilateral correlations with the thalamus and insula, as well as contralateral correlations are not apparent for MB 8 and higher in preprocessing without temporal filtering (A). These biases are reduced with bandpass filtering (B), which results in clear left-right putamen functional connectivity in MB 2 to MB 8. Effect sizes are larger in single-band 3.3 mm.

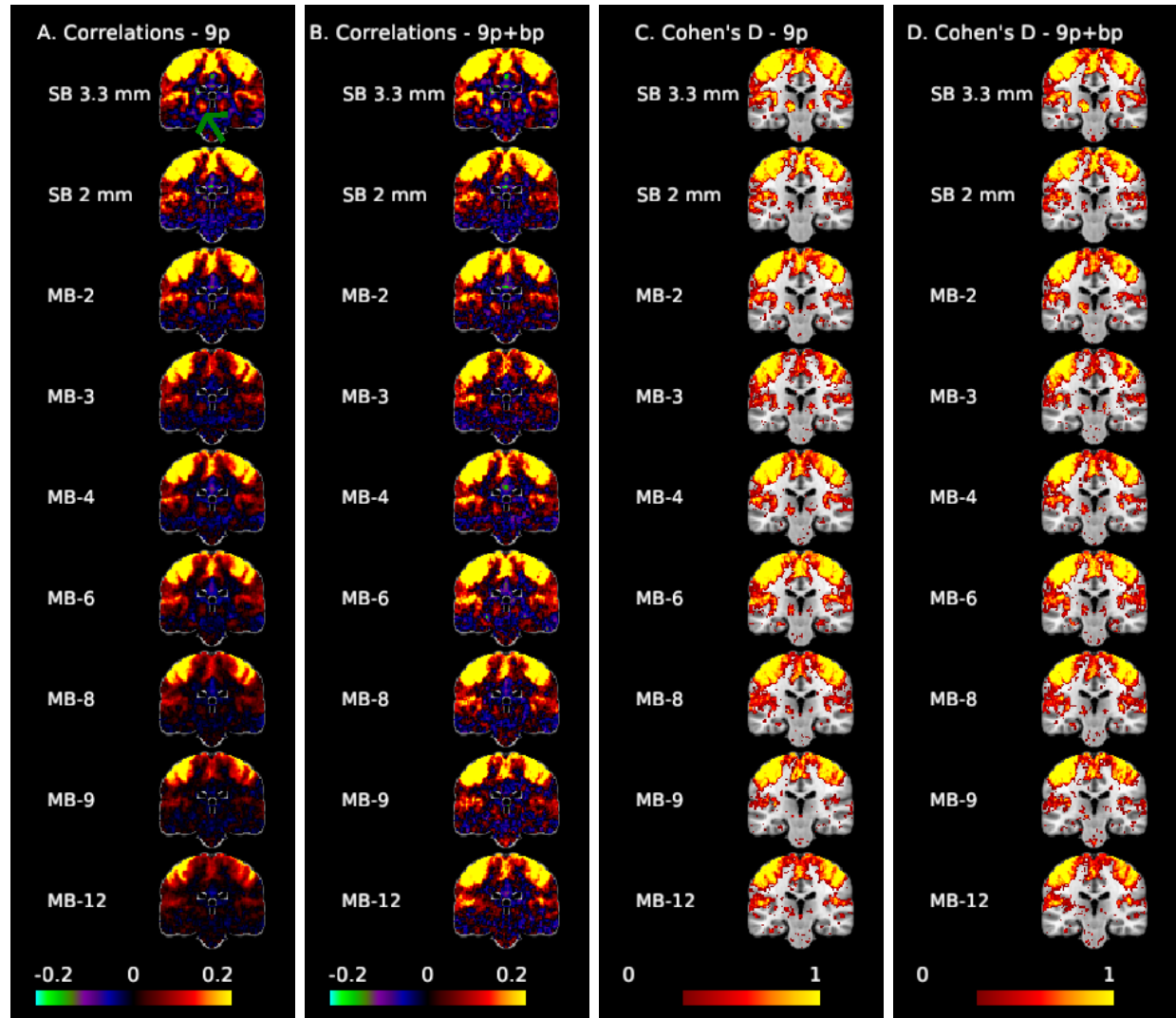


Figure 3: Correlation (A,B) and Cohen's d maps thresholded to display values >0.3 (C,D) for the motor seed (MNI: -41, -20, 62) at coronal slice -24 to examine motor-thalamic pathways. The green arrow points to the thalamus. Thalamocortical connectivity is clearly apparent in the SB 3.3 mm acquisition, with smaller but notable effect sizes in the MB 2 to MB 6 acquisitions.

481 Web Supplement Figure S.6, this area is only faintly apparent in most acquisitions in 9p,
482 with largest correlations at MB 2 (around 0.10), most acquisitions around 0.05, and small or
483 negligible correlations in SB 2 mm and MB 12. The region is more apparent in 9p+bandpass,
484 with correlations greater than 0.10 for SB 3.3, MB 2, 3, 4, 6, 8, and 9, but are poorly captured
485 at SB 2 mm and MB 12. In the Cohen's d maps (Web Supplement Figure S.7), these areas
486 are best represented by MB 2 in both 9p and 9p+bandpass, with comparable spatial extents
487 from MB 2 to MB 8. The effect sizes in this region of the cerebellum for SB 3.3 mm are
488 smaller than MB 2 to MB 8. This implies that there is not a single optimal MB factor for
489 seed maps, but the general pattern is that SB 3.3 mm performs better in areas with high
490 g -factor and MB 2 to 6 in areas with moderate and low g -factor.

491 4.3. Impacts on pairwise correlations in a functional atlas

492 4.3.1. Impacts on the magnitude of correlations

493 Higher standard deviations in multiband acquisitions led to smaller correlations in the
494 9p pipeline, and bandpass filtering reduced g^* -factors to result in greater similarity across
495 acquisitions. Figure 4 depicts scatterplots of the correlations for each edge at a given MB
496 factor versus the correlation for the SB 2 mm acquisition. Each data point corresponds to
497 the average of the Fisher z-transformed correlations for an edge in the 264-node atlas. The
498 points are colored according to their g^* -factor, where the color scale varies from a g^* -factor
499 of one in blue, which represents no noise amplification relative to SB 2 mm, to four in red,
500 in which the denominator in the correlation is approximately four times larger in the MB
501 acquisition than SB 2 mm. In the absence of multiband impacts, we expect the points to
502 lie approximately along the line $y = x$. In the positive quadrant $x > 0, y > 0$, points below
503 the line $y = x$ indicate correlations that are smaller in the MB acquisition along the y-axis
504 than in the SB 2 mm; similarly, points above the line $y = x$ in the quadrant $x < 0, y < 0$
505 represent smaller correlations relative to SB 2 mm.

506 In the 9p pipeline (left column), we see that at higher MB factors, the g^* -factors are
507 larger, and points with high g -factors tend to lie closer to the line $y = 0$. This provides

508 evidence that noise amplification can lead to smaller correlations.

509 In the 9p+bandpass (right column), we see that overall the g^* -factors are closer to one,
510 even at higher MB factors, and the points tend to fall closer to the line $y = x$. This indicates
511 that the correlations are now more comparable across MB factors.

512 Using generalized additive mixed models to statistically test these patterns, we observed
513 that increased g^* -factors did, in fact, significantly decrease correlations for the subset of
514 edges described in Section [3.5.1 Impacts on the magnitude of correlations](#) ($p < 0.001$). For
515 example, a Fisher z-correlation equal to 0.35 decreased to approximately 0.05 for g^* -factor=1
516 versus g^* -factor=8 when controlling for edge, gender, and scanner (Figure 5). Note gender
517 and scanner were not significant ($p > 0.05$).

518 Examining plots of the correlation matrices sorted by community allows us to explore
519 where these impacts occur (Figure 6). For 9p processed data (upper diagonals in Figure
520 6), we see that the effects of acceleration differ across space. A close inspection reveals
521 that when comparing the upper diagonal in MB 4 to the upper diagonal in MB 8, intra-
522 and inter-community correlations involving salience, auditory, cingulo-opercular task control,
523 somatomotor, and subcortical regions tend to be smaller in MB 8 than MB 4. In contrast,
524 correlations are more comparable within the visual system across most acquisitions. A
525 focused view on subcortical and cerebellar ROIs reveals large decreases in correlations when
526 no temporal filtering is applied (upper diagonal of Web Supplement Figure S.8). Many
527 correlations exceed 0.3 in SB and MB 2 to 4, but these correlations are decreased in MB 8
528 to MB 12.

529 In contrast, correlations in the 9p+bandpass processed data (lower diagonals in Figure 6)
530 appear similar across MB acquisition. A close inspection indicates that SB 3.3 mm has the
531 highest correlations within subcortical and within cerebellum, and correlations are somewhat
532 reduced in MB 8 to MB 12 (Web Supplement Figure S.8). In general, temporal filtering tends
533 to increase correlations in MB accelerations, with relatively minor effects for SB and MB 2.

534 Next, we narrowed our focus to edges expected to have positive correlations (as described

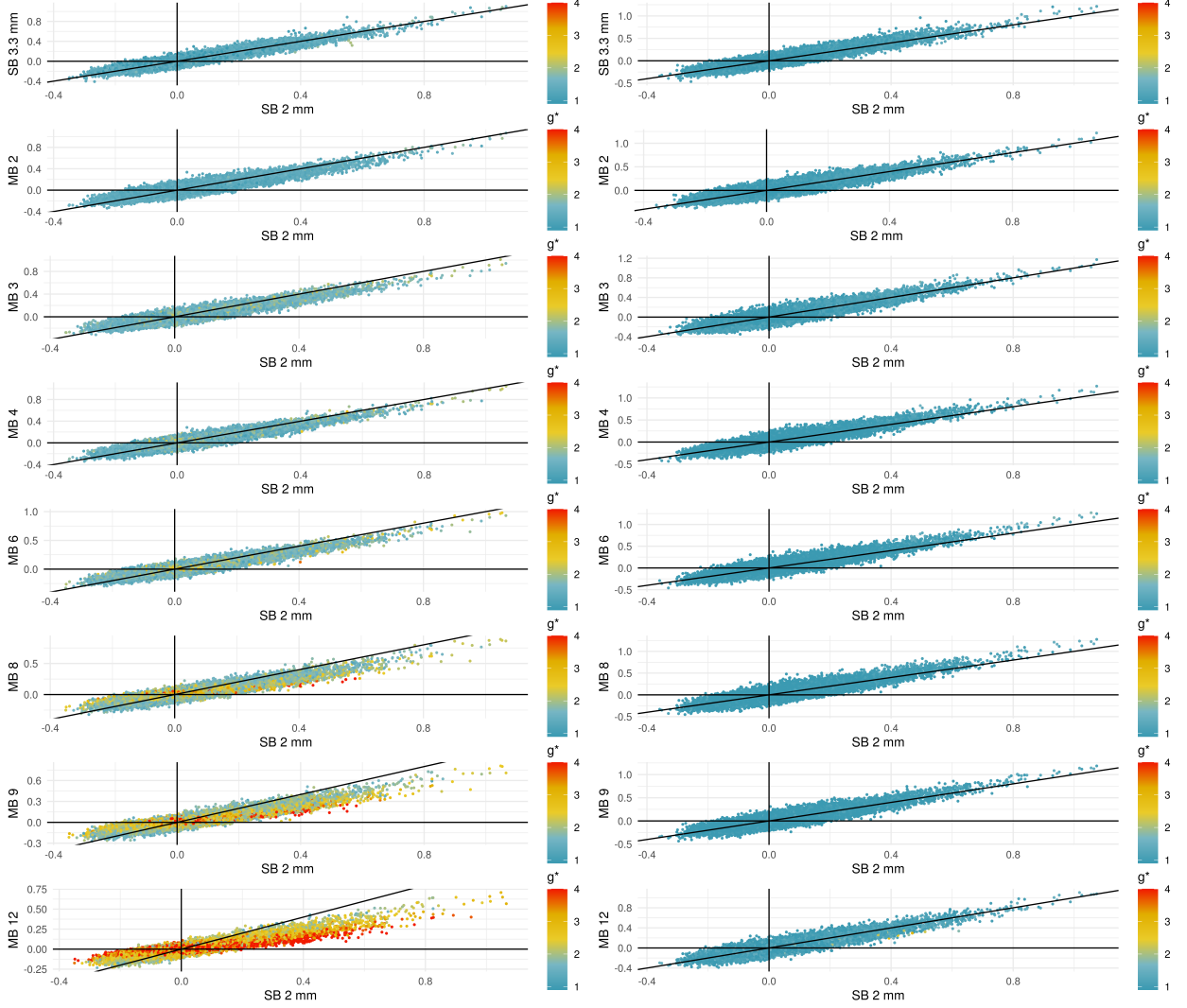


Figure 4: Scatterplots comparing correlations in SB to different MB acquisitions using 9p processing (left) and 9p+bandpass (right). The black line occurs at $y = x$, and points below the line in the quadrant $x > 0$, $y > 0$ represent positive correlations that are attenuated in the MB acquisition. Points above the line in $x < 0$, $y < 0$ represent negative correlations that are attenuated at the higher MB factors. Points are colored by their g^* -factors, which are defined for each pipeline; see (6). In the 9p pipeline, the g^* -factors are larger at higher MB factors, and points with high g -factors tend to lie closer to the line $y = 0$. In the 9p+bandpass, the g^* -factors are closer to one, even at higher MB factors, and the points tend to fall closer to the line $y = x$.

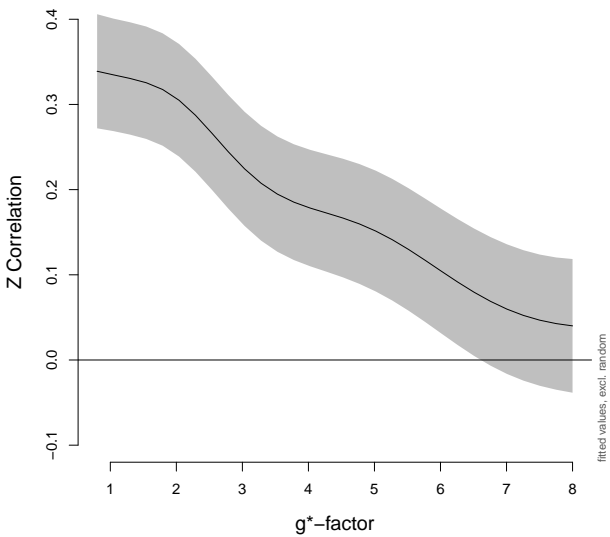


Figure 5: Correlations decrease as noise amplification increases. Fisher z-transformed correlations in a subset of edges that were a priori expected to have positive correlations, as described in Section 3.5.1 *Impacts on the magnitude of correlations*, were analyzed using a generalized additive mixed model. The overall effect of g^* -factor was highly significant ($p < 0.001$). The GAMM includes a smoother for g^* -factor with penalty selected using REML, fixed effects for edge, gender, and scanner, and random effects for participant and participant \times edge. The y-intercept in this figure corresponds to the edge with median correlation (nodes 92 and 109, default mode). Gray indicates point-wise 95% confidence intervals.

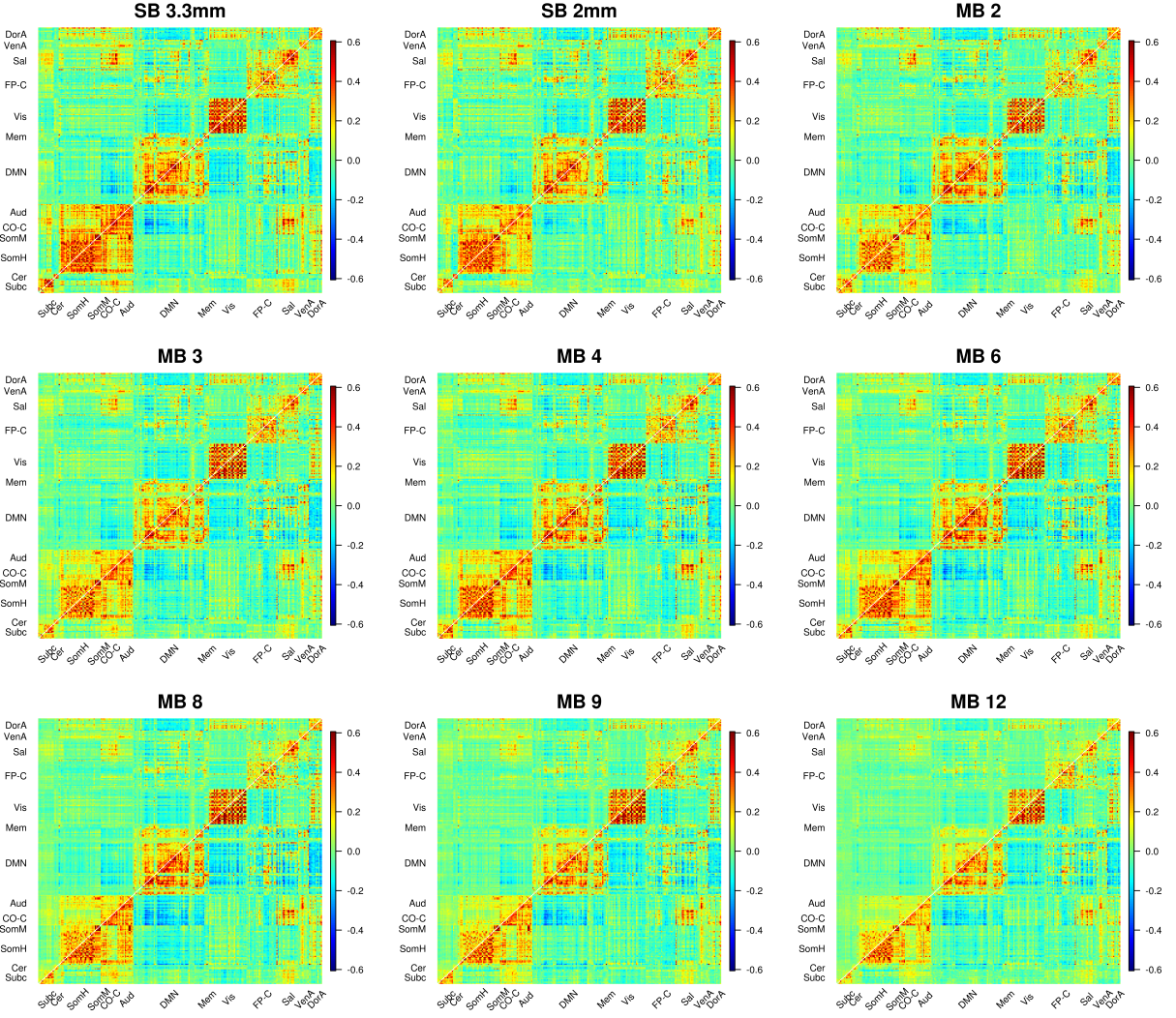


Figure 6: Average correlations (Fisher z-transformed) for SB and MB acquisitions. 9p processing is above the diagonal and 9p+bandpass below. In 9p, the effects of acceleration differ across space, e.g., we see smaller correlations involving salience, auditory, cingulo-opercular task control, and subcortical regions in MB 12 than MB 4; a close inspection reveals MB 8 also tends to be lower than MB 4 in these edges. In contrast, correlations are more comparable within the visual system across most acquisitions. In 9p+bandpass, the correlations across MB factor are more similar (below diagonal). Web Supplement Figure S.8 depicts a zoomed in version of subcortical and cerebellar edges that more clearly illustrates lower correlations at higher MB factors for these regions. Web Supplement S.9 and S.10 illustrate impacts on edges that are expected to have positive correlations.

	Thalamus - 9p	Putamen - 9p	Cerebellum - 9p	Executive - 9p	Salience - 9p	DMN - 9p
Int.	0.54(0.05)	0.59(0.05)	0.29(0.04)	0.39(0.03)	0.29(0.03)	0.43(0.03)
SB3.3	0.34(0.07) <.001	0.22(0.05) <.001	-0.04(0.04) 0.37	0.01(0.03) 0.857	0.03(0.03) 0.239	0.04(0.04) 0.276
MB 2	0.07(0.05) 0.186	0.01(0.04) 0.862	-0.03(0.04) 0.432	-0.09(0.03) 0.007	0.01(0.03) 0.751	-0.02(0.03) 0.59
MB 3	-0.05(0.06) 0.427	-0.1(0.04) 0.008	-0.09(0.04) 0.024	-0.09(0.03) 0.001	-0.03(0.03) 0.346	-0.06(0.03) 0.049
MB 4	0.02(0.05) 0.669	-0.11(0.04) 0.003	-0.1(0.04) 0.007	-0.06(0.03) 0.026	-0.03(0.03) 0.271	-0.07(0.03) 0.007
MB 6	-0.08(0.05) 0.119	-0.17(0.04) <.001	-0.12(0.04) 0.002	-0.1(0.03) 0.001	-0.05(0.03) 0.032	-0.07(0.03) 0.032
MB 8	-0.31(0.05) <.001	-0.32(0.04) <.001	-0.19(0.03) <.001	-0.13(0.03) <.001	-0.08(0.02) 0.001	-0.14(0.02) <.001
MB 9	-0.3(0.05) <.001	-0.34(0.04) <.001	-0.23(0.03) <.001	-0.14(0.03) <.001	-0.1(0.02) <.001	-0.17(0.03) <.001
MB 12	-0.36(0.05) <.001	-0.44(0.03) <.001	-0.21(0.03) <.001	-0.18(0.02) <.001	-0.16(0.02) <.001	-0.25(0.03) <.001
	Thalamus - 9p+bp	Putamen - 9p+bp	Cerebellum - 9p+bp	Executive - 9p+bp	Salience - 9p+bp	DMN - 9p+bp
Int.	0.52(0.06)	0.59(0.06)	0.31(0.04)	0.39(0.04)	0.26(0.04)	0.43(0.04)
SB3.3	0.47(0.07) <.001	0.31(0.05) <.001	-0.02(0.04) 0.637	0.04(0.04) 0.249	0.08(0.03) 0.01	0.11(0.04) 0.006
MB 2	0.22(0.05) <.001	0.1(0.05) 0.036	-0.01(0.04) 0.814	-0.06(0.04) 0.167	0.05(0.03) 0.115	0.04(0.03) 0.172
MB 3	0.22(0.07) 0.001	0.09(0.05) 0.051	0(0.06) 0.98	-0.03(0.04) 0.417	0.05(0.04) 0.201	0.04(0.03) 0.228
MB 4	0.33(0.06) <.001	0.18(0.04) <.001	-0.01(0.04) 0.87	0.04(0.04) 0.362	0.07(0.03) 0.032	0.03(0.03) 0.287
MB 6	0.29(0.06) <.001	0.14(0.06) 0.012	-0.02(0.05) 0.746	-0.02(0.04) 0.543	0.06(0.03) 0.052	0.1(0.04) 0.008
MB 8	0.07(0.05) 0.207	0.07(0.05) 0.133	-0.09(0.04) 0.021	-0.03(0.04) 0.342	0.07(0.03) 0.038	0.06(0.03) 0.054
MB 9	0.09(0.07) 0.151	0.06(0.06) 0.276	-0.08(0.05) 0.133	-0.03(0.04) 0.433	0.06(0.03) 0.071	0.01(0.04) 0.712
MB 12	0.04(0.06) 0.442	-0.12(0.05) 0.025	-0.1(0.05) 0.081	-0.02(0.04) 0.677	-0.02(0.03) 0.604	-0.04(0.03) 0.246

Table 2: Impact of MB factor on Fisher z-transformed correlations for selected edges (see Section 3.5 *Impacts on pairwise correlations in a functional atlas*). Estimates, standard errors, and p-values (uncorrected) from generalized estimating equations with robust standard errors. The intercept is the average Fisher z-transformed correlation for edges in the indicated community for SB 2 mm controlling for gender and scanner. P-values represent whether the correlation of the acquisition differs significantly from SB 2 mm. Differences with $p \leq 0.001$ are in bold and colored red for acquisitions significantly lower than 2 mm and blue for acquisitions significantly higher. Top: 9p. Bottom: 9p+bandpass.

in Section 3.5.1 *Impacts on the magnitude of correlations*). In the 9p processed data, we observed large differences between the SB 2 mm acquisition and other acquisitions, with Fisher z-transformed correlations tending to decrease as MB factor increases for all communities (Table 2 and Web Supplement Figure S.9). Correlations were lower in MB 8, MB 9, and MB 12 compared to SB 2 mm for all communities ($p \leq 0.001$). These decreases were most prominent in the thalamus and putamen, and in particular the impacts were more severe when the g^* -factors were higher (Web Supplement Figure S.9). In the thalamus, MB 2 to 6 correlations were comparable to SB 2 mm correlations ($p > 0.05$). The putamen appears more sensitive to MB acquisitions than the thalamus, as MB 3 to MB 6 correlations were lower than SB 2 mm ($p < 0.01$) in addition to MB 8 to MB 12. Correlations involving the thalamus and putamen were higher in SB 3.3 mm data compared to SB 2 mm data ($p < 0.001$).

Web Supplement Figure S.9 also reveals a large degree of inter-subject variation in correlations, as well as some degree of inter-subject variation in g^* -factors. For example, in the thalamus at MB 6, participants' g^* -factors vary from 1.31 to 7.57, where the g^* -factors are more variable in regions that on average have higher g^* -factors.

551 As was the case for the full set of edges, correlations were in general more similar across
552 MB acquisitions for the 9p+bandpass processed data, but there were some notable differences
553 in subcortical regions (Table 2). In the thalamus, SB 3.3 mm was much higher and MB 2 to
554 6 notably higher than SB 2 mm ($p \leq 0.001$). In the putamen, SB 3.3 mm and MB 4 were
555 higher than SB 2 mm ($p < 0.001$). The correlations across acquisitions in the cerebellum
556 were generally similar to SB 2 mm with a trend of lower correlations in MB 8, MB 9, and MB
557 12 ($p = 0.02$, $p = 0.13$, $p = 0.08$, respectively). Correlations were similar to SB 2 mm within
558 executive control. In salience, SB 3.3 mm tended to have higher correlations (0.08 on Fisher
559 z-scale, $p = 0.01$). In the default mode network (DMN), SB 3.3 mm and MB 6 tended to have
560 higher correlations (0.1 on Fisher z-scale, $p < 0.01$). Boxplots with participant data colored
561 by g^* -factor appear in Web Supplement Figure S.10, which illustrates that correlations
562 overall are similar across acquisitions, with the notable exception of higher correlations at
563 SB 3.3 mm and MB 4 compared to other acquisitions in the thalamus and putamen.

564 In the 9p+spatial smoothing and 9p+bandpass+spatial smoothing, the patterns were
565 similar to the 9p and 9p+bandpass, respectively (Web Supplement Table S.1). Overall, the
566 correlations tended to be higher in smoothed data compared to the unsmoothed data.

567 4.3.2. Impacts on edge density

568 The number of significant correlations (edge density) with 9p preprocessing tended to
569 be higher in MB 6, MB 4, and MB 8, with the relative ranking of SB 3.3 mm depending
570 on the community, and SB 2 mm, MB 2, MB 3, MB 9, and MB 12 tending to perform
571 worse (Figure 7A). MB 6 had the greatest edge density across all edges, and MB 8 was
572 nearly equal (difference between MB 6 and MB 8=0.006, $p = 0.46$; all differences and p-
573 values hereafter are relative to MB 8, Web Supplement Table S.2), and MB 4 also nearly
574 equal (difference=0.001, $p = 0.95$). The next highest density was MB 3 (difference=-0.011,
575 $p = 0.15$) followed by SB 3.3 mm (difference=-0.014, $p = 0.05$), with lower densities in
576 MB 9, MB 2, SB 2 mm, and MB 12 ($p < 0.004$). Edge density was somewhat higher in
577 MB 4 and MB 6 than MB 8 for edges with a subcortical node (difference=0.026, $p = 0.06$,

and difference=0.028, $p = 0.07$, respectively) and for fronto-parietal task control ($p = 0.06$, $p = 0.01$, respectively). The ranking of the proportion of significant correlations in SB 3.3 mm varied by community, with lower densities for default mode and visual compared to MB 8 (difference=-0.043, $p = 0.001$ and diff=-0.023, $p = 0.01$, respectively), while in subcortical, the density in SB 3.3 mm was close to MB 4 and MB 6 (Figure 7A) with a trend of higher density than MB 8 (difference=0.023, $p = 0.10$). Note the power of the permutation test is impacted by the size of the community (e.g., 31 nodes in visual versus 13 nodes in subcortical).

Overall, spatial smoothing did not impact the relative rankings of the MB factors. Permutation tests for 9p+spatial smoothing were similar to 9p (Web Supplement Table S.3). The overall pattern is that MB4, MB 6, and MB 8 outperform SB 2 mm, MB 2, and MB 12.

The number of significant correlations with 9p+bandpass across all edges was highest in MB 8, with approximately equal density in MB 6 ($p = 0.92$) and similar density in MB 4 ($p = 0.49$) (Figure 7, Web Supplement Table S.4). Across all edges, the rankings were similar to 9p, in which SB 3.3 mm and MB 3 were somewhat lower than MB 8 (difference=-0.012, $p = 0.08$ and difference=-0.012, $p = 0.10$), and SB 2 mm, MB 2, MB 9, and MB 12 lower (differences larger than -0.02, $p < 0.003$). In contrast to the trends in 9p, subcortical density was similar in MB 8 versus SB 3.3 mm, MB 4, and MB 6 ($p \geq 0.30$).

There were fewer significant edges in 9p+bandpass compared to 9p across most communities and acquisitions (Web Supplement Table S.5). This included the densities across all edges ($p < 0.001$ for all acquisitions except MB 8 and MB 12, where $p = 0.02$ and $p = 0.26$, respectively). The overall reduced edge density in 9p+bandpass may be due to removing signal (decrease in power) and/or removing physiological confounding (decrease in false positives, where here we consider a true positive if the connection is due to neural signal); see Section 5.3 *Temporal filtering decreases noise amplification and physiological signal but may remove neural signal*.

Plots of the matrices of Cohen's d illustrate that effect size matrices look somewhat

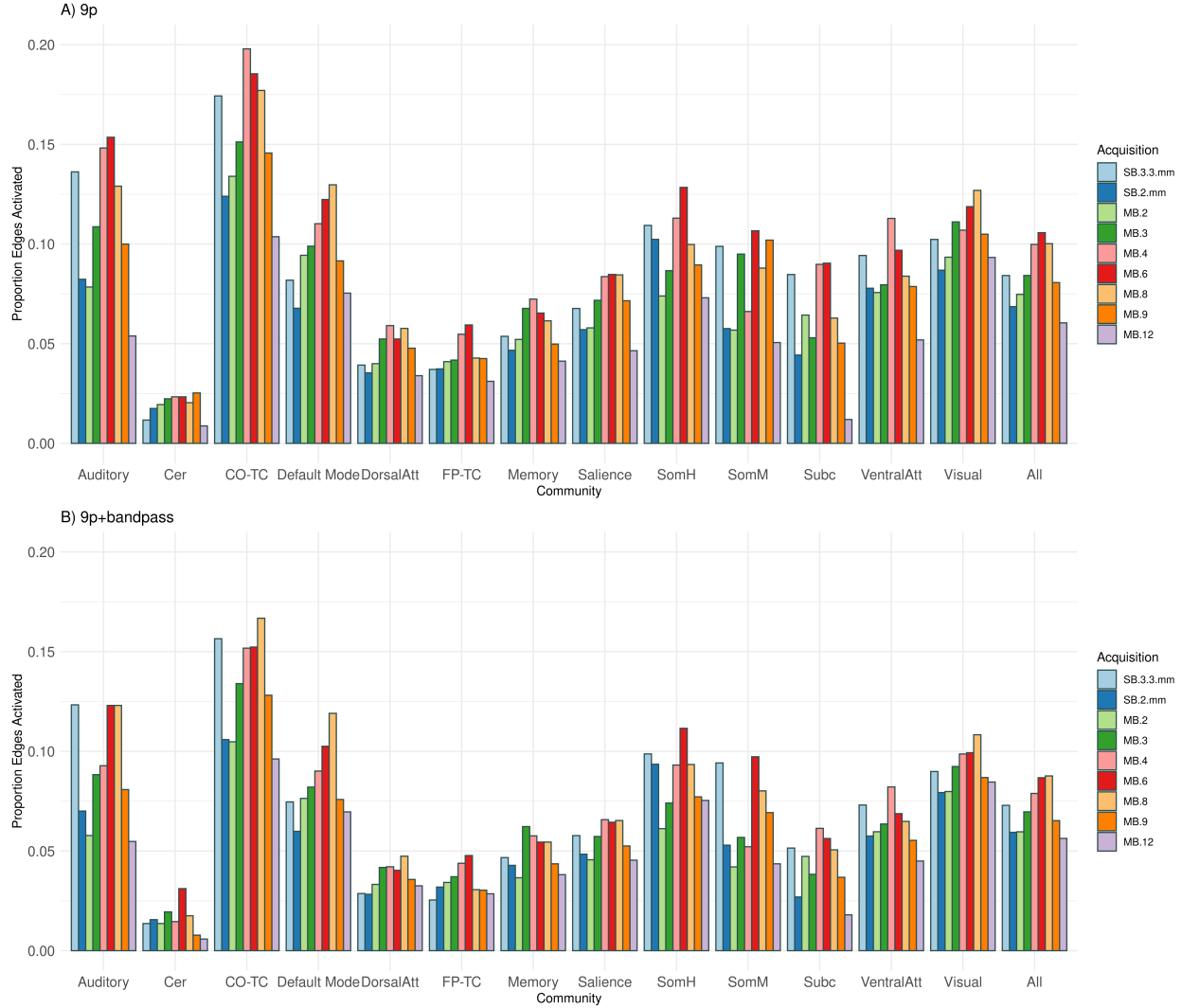


Figure 7: Edge density (number of significant correlations) for thirteen communities (auditory, cerebellum, cingulo-opercular task control, default mode, dorsal attention, fronto-parietal task control, memory, salience, somatomotor hand, somatomotor mouth, subcortical, ventral attention, and visual) and across all edges (all). The edge density for a community is defined as the proportion of significant one-sample t-statistics (using the Bonferroni-corrected α -level) for the Fisher z-transformed correlations for each edge in which at least one of the nodes is in the community. A) The number of significant correlations with 9p preprocessing tended to be higher in MB 6, MB 4, and MB 8, with the relative ranking of SB 3.3 mm depending on the community, and SB 2 mm, MB 2, MB 3, MB 9, and MB 12 tending to perform worse. Permutation tests of significant differences between MB factors appear in Web Supplement Table S.2. Similar results were obtained with 9p+spatial smoothing, shown in Web Supplement Table S.3. B) The rankings with 9p+bandpass were similar to 9p, with MB 8, 6 and 4 tending to be higher than others and SB 2 mm, MB 2, MB 9, and MB 12 lower. Permutation tests of significant differences between MB factors appear in Web Supplement Table S.4. Overall, 9p+bandpass had lower edge density compared to 9p, with significant differences displayed in Web Supplement Table S.5.

similar across many acquisitions with some notable differences (Figure 8). The subcortical to salience connections tend to be stronger in MB 4 and MB 6, particularly when compared to MB 3 and MB 9. Visually, Cohen's d in 9p and 9p+bandpass look more comparable. In fact, the effect sizes tend to be higher with 9p preprocessing; as discussed above, the number of significant correlations was higher in 9p than 9p+bandpass in nearly all communities and MB factors (Web Supplement Table S.5).

4.4. Impacts in independent datasets

4.4.1. Evaluation of a third scanner using a 64-channel head coil

In the three subjects collected with the 64-channel head coil and scanner at the University of Rochester, we observed similar patterns of noise amplification as in the Emory cohort (Web Supplement S.12). In particular, we do not see any clear evidence of large differences due to different head coils.

In the seed maps for the right dorsal rostral putamen, we again see the general pattern that correlations decrease as MB factor increases, and temporal filtering reduces these biases (Web Supplement S.13). An exception to the decreasing trend in correlations with MB factor is that MB 4 had higher correlations than MB 3. In this small sample, these patterns are more clearly illustrated with the spatially smoothed data (panels C and D). In 9p+spatial smoothing, correlations with the left putamen appear stronger in SB 3.3 mm, MB 2, and MB 4 compared to the other acquisitions. In 9p+bandpass+spatial smoothing, MB 4 appears to most clearly reveal right-left connectivity.

In the correlation matrices, we also see a trend of decreasing correlations with increasing multiband factor with 9p processing, whereas acquisitions appear more similar with 9p+bandpass processing (Web Supplement Figure S.14).

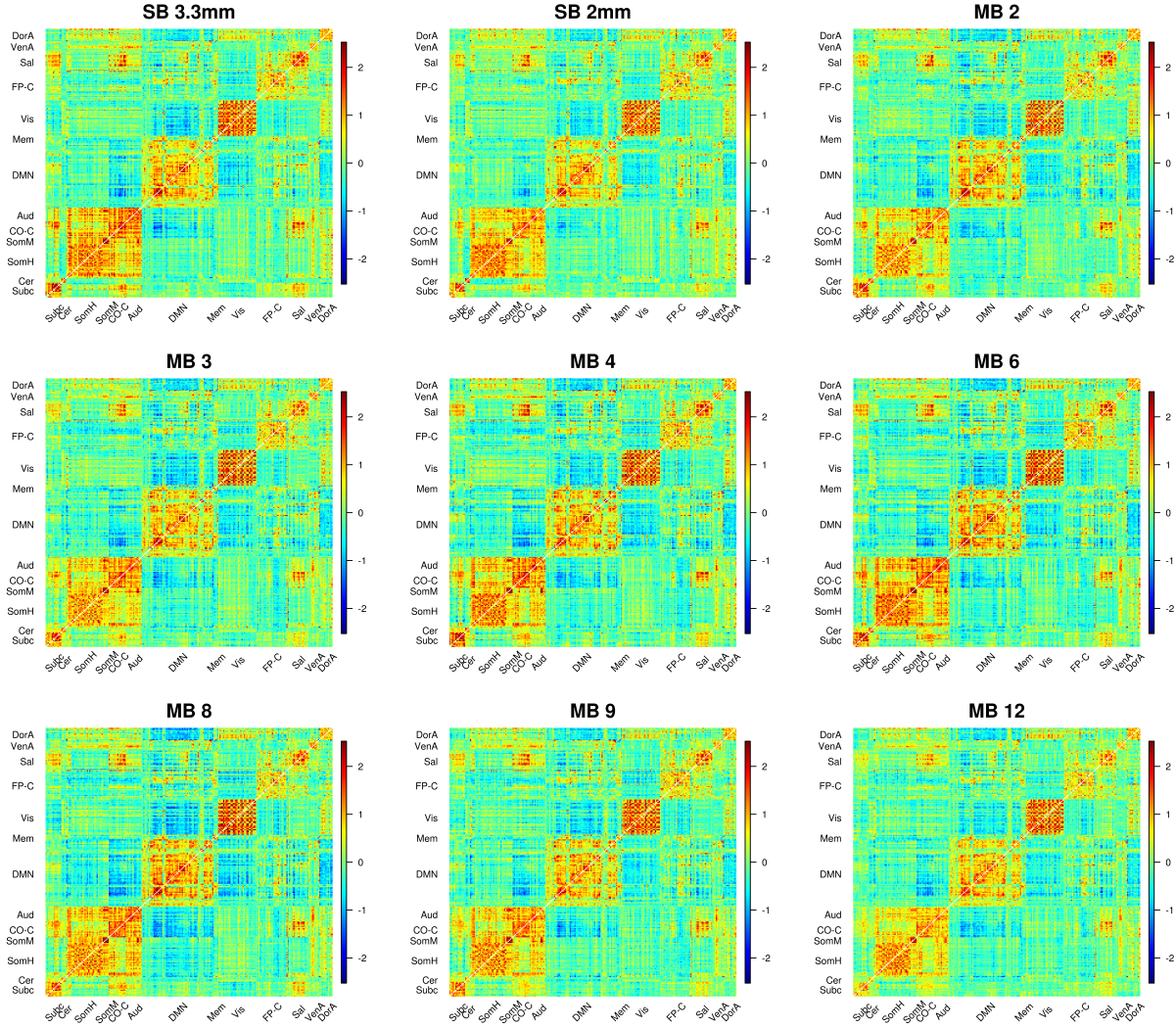


Figure 8: Cohen's d for SB and MB acquisitions. Cohen's d statistic is formed for the one-sample t-test of the null hypothesis that the Fisher z-transformed correlation is equal to zero. Cohen's d for 9p preprocessing is above the diagonal and 9p+bandpass below the diagonal. Compared to the correlations in Figure 6, effect size matrices in 9p and 9p+bandpass look more similar. A close examination reveals some differences. For example, the subcortical to salience connections tend to be stronger in MB 4 and MB 6 than MB 3 and MB 9 in 9p, and these effect sizes tend to be reduced in 9p+bandpass. In general, there were some significant differences between MB factors, as illustrated in Web Supplement Tables S.2 and S.4, and 9p+bandpass tended to have lower effect sizes than 9p, as illustrated in Web Supplement Table S.5.

628 4.4.2. *Evaluation of pairwise correlations in the preprocessed Young Adult Human Connec-
629 tome Project data*

630 In the ICA-FIX rs-fMRI data from the HCP (collected using MB 8), we see that many
631 subcortical to subcortical and subcortical to cortical correlations appear weak in the corre-
632 lation matrix. In contrast, functional connectivity between these regions is more prominent
633 in the Cohen's d matrix (Web Supplement [S.4.2](#)).

634 **5. Discussion**

635 We evaluated the impact of multiband acceleration on correlation-based functional con-
636 nectivity using MB factors of 2, 3, 4, 6, 8, 9, and 12 with 2 mm isotropic voxels, and
637 additionally 2 mm and 3.3 mm single-band acquisitions. Our contributions are the follow-
638 ing:

- 639 1. In seed maps, putamen connectivity and motor-thalamic connectivity were both higher
640 in the single-band 3.3 mm acquisition (both with and without bandpass), with MB 4
641 performing well among 2 mm acquisitions.
- 642 2. Noise amplification from multiband acceleration creates large spatial biases in corre-
643 lations, suggesting underestimated subcortical-cortical connectivity, particularly at high
644 MB factors (8 and higher).
- 645 3. Bandpass filtering decreases spatial biases but in some settings reduces effect sizes.
- 646 4. Effect sizes or test statistics should be used for multiband studies, and correlations
647 without noise removal should not be reported.
- 648 5. MB 4, 6 and 8 have a greater number of significant correlations across a functional
649 atlas (both with and without bandpass), with lower edge density in SB 2 mm, MB 2,
650 MB 9, and MB 12.

651 We discuss our recommendations and study limitations below.

652 5.1. Recommendations

653 In our seed-based analysis, we examined functional connectivity between locations where
654 we expect true functional connectivity based on anatomy and previous studies. Our rec-
655 ommendation is to use SB 3.3 mm for seed-based connectivity studies where the regions of
656 interest fall in high g -factor areas, and we recommend MB 4 for 2 mm acquisitions. For a
657 seed in the right putamen (high g -factor), bilateral putamen connectivity and connections
658 to the insula, cingulate, and thalamus were clearly more prominent in SB 3.3 mm than other
659 acquisitions, and bandpass filtering did not impact this conclusion (Figure 2). Among the
660 2 mm acquisitions, connectivity in MB 4 was higher than others, particularly for putamen-
661 thalamic connectivity. For the correlations between a seed in the motor cortex (low g -factor)
662 and the thalamus (high g -factor), this pathway is also best captured using the SB 3.3 mm
663 acquisition (Figure 3). In particular, MB 8 and higher do not robustly reveal this thalam-
664 ocortical connectivity. The pathway between the motor cortex and cerebellum (moderate
665 g -factor) is best captured using MB 4 (Web Supplement Figure S.7).

666 In the analyses of correlations between regions in a functional atlas, our results indicate
667 that the number of significant correlations is on average higher in MB 6, MB 8, and MB 4
668 compared to other acquisitions (Figure 7, Web Supplement Table S.2). All acquisitions have
669 a decreased number of significant correlations in 9p+bandpass compared to 9p. Overall, we
670 prefer MB 4 compared to MB 6 and MB 8 because it performs comparably in the functional
671 atlas analysis, and it has benefits in subcortical seed-based analyses.

672 We recommend reporting effect sizes, or similarly, test statistics, in resting-state studies
673 utilizing multiband data, including secondary analyses of existing data. Correlations are
674 reduced in regions with noise amplification in multiband (Figures 2, 3, 4; Web Supplement
675 Figures S.8, S.9.) If correlations (rather than effect sizes or test statistics) are reported,
676 noise removal, e.g., temporal filtering, can reduce spatial biases, but may also have costs.
677 We discuss temporal filtering in Section 5.3 *Temporal filtering decreases noise amplification*
678 *and physiological signal but may remove neural signal.*

679 This study used young, healthy subjects and one-sample tests. We expect that these
680 results also apply to comparing groups, e.g., disease versus healthy. In disease versus healthy,
681 g -factors will attenuate the differences in a manner parallel to the one-sample analysis (see
682 Section [2.1 Noise amplification and functional connectivity](#)). Thus we also recommend MB
683 4 for whole-brain group comparisons, and SB 3.3 mm for seed-based analyses of subcortical
684 functional connectivity.

685 *5.2. Generalizability*

686 Decisions at every step in the study design process could potentially impact our findings,
687 but we made these decisions in a way to improve the generalizability of our recommendations.
688 First, the combination of scanner model and head coil used in our Emory cohort (Siemens
689 PrismaFit, 32-channel head coil) are amongst the most commonly used in recent rs-fMRI
690 studies. Thus our findings are widely applicable to many other research labs. Secondly,
691 we chose to use standard, popular preprocessing pipelines commonly found in the literature
692 ([Ciric et al., 2017](#); [Parkes et al., 2018](#)), rather than specialized or less common processing
693 pipelines, which arguably improves the generalizability of the results.

694 The spatial biases in correlations are a general issue in multiband acquisitions that is
695 expected to be problematic across scanner types and head coils. This includes secondary
696 analyses of the UK BioBank ([Miller et al., 2016a](#)), HCP ([Glasser et al., 2013](#); [Howell et al.,
697 2019](#)), ABCD ([Hagler et al., 2019](#)), ADNI-3 ([Weiner et al., 2017b](#)), and other public datasets.
698 Noise amplification is a cost of multiband acquisition ([Setsompop et al., 2012](#); [Xu et al.,
699 2013](#); [Todd et al., 2017](#); [Risk et al., 2018](#)). Consistent with the theoretical arguments in (3),
700 we empirically showed correlations were reduced in regions with high noise amplification.
701 This was true for the expected connection between LM1 and the thalamus in our seed map
702 analysis (Figure 3). It emerged as a general pattern when we examined the impact of g *-
703 factors on correlation magnitude using the Power 264-node functional atlas (Figure 5). We
704 also saw this pattern in the 64-channel head coil used in the University of Rochester cohort
705 (Web Supplement Figures [S.13](#) and [S.14](#)). We again observed evidence that effect sizes may

706 capture functional connectivity involving subcortical areas in our secondary analysis of the
707 HCP data (Web Supplement Figure S.15).

708 *5.3. Temporal filtering decreases noise amplification and physiological signal but may remove*
709 *neural signal*

710 Temporal filtering in multiband acquisitions has three impacts: 1) a reduction in noise
711 amplification; 2) a reduction in physiological sources of correlation; and 3) a possible intro-
712 duction of bias due to the removal of neural signal. Figure 1 shows temporal filtering results
713 in dramatic reductions in noise amplification, which increases correlations. However, the
714 increase in correlations does not result in an increase in power because of the loss of residual
715 degrees of freedom, resulting in the same degrees of freedom across MB factors (Table 1).

716 We implement bandpass filtering during nuisance regression in the temporal domain using
717 AFNI’s 3dTproject. Lindquist et al. (2019) and Hallquist et al. (2013) found that imple-
718 menting temporal filtering and nuisance regression in separate steps led to biased results.
719 Intuitively, low-pass filtering removes all the high frequency content from data, which ren-
720 ders it more similar to slower acquisitions. This includes a removal of some of the effects
721 of noise amplification, as well as some cardiac and respiratory effects because most of their
722 power resides outside the passband.

723 The reduction in variance due to physiological sources is depicted in Figure 1, in which
724 the contributions of physiological noise steadily decline with increase in MB factor. The
725 overall number of significant edges decreased when using temporal filtering (Web Supple-
726 ment Table S.5, Figure 7). An important limitation in our brain-wide analysis is that we
727 do not distinguish between true positives and false positives, where false positives include
728 high correlations from motion and physiology. However, our seed-based analysis provides
729 some insight into neural effects that may be reduced by bandpass filtering. Tract-tracing
730 studies have established the existence of cortical projections between the dorsal anterior cin-
731 gulate and the striatum, including the putamen (Haber et al., 2006). Consistent with this
732 anatomical evidence, we observed weak, but notable, correlations between the putamen and

733 cingulate in SB 3.3 mm data, but these correlations were decreased by bandpass filtering
734 (Figure 2). Tract-tracing and physiological experiments have also revealed the presence of
735 projections from the thalamus to the putamen (Haber and Calzavara, 2009), but in the
736 present study, functional connectivity evidence of these projections appears to have been
737 reduced by bandpass filtering in MB 6 and MB 8. Feinberg et al. (2010) and Lee et al.
738 (2013) suggest there is neural signal in the high-frequency content of MB acquisitions, which
739 may be discarded by bandpass filtering. Jahanian et al. (2019) also found benefits of MB 6
740 without temporal filtering in their study comparing MB 6 to SB. Chen et al. (2019) caution
741 that temporal filtering is not a catch-all for cardiac and respiratory effects, as these effects
742 are not sinusoidal and contain higher order harmonics.

743 *5.4. Preprocessing pipelines and strategies for artifact and noise removal*

744 We examined four preprocessing pipelines in which all pipelines included a popular and
745 effective approach to nuisance regression (white matter, CSF, global signal, and the 6 pa-
746 rameters from motion regression) (Ciric et al., 2017; Parkes et al., 2018; Fox et al., 2005,
747 2009), and we compared results with and without temporal filtering, as well as with and
748 without spatial smoothing. The possible benefits of multiband with alternative preprocess-
749 ing pipelines is an important avenue for future research. Data from this study are available
750 on OpenNeuro (<https://openneuro.org/datasets/ds003540>) to facilitate studies on the
751 impacts of preprocessing.

752 While GSR is effective at minimizing respiratory as well as motion-related artifacts, more
753 targeted physiological noise removal strategies may help leverage the benefits of higher sam-
754 pling rates. Fair et al. (2020) found that notch filters to target the respiratory rate improved
755 fMRI data quality, particularly in multiband data. For studies that collect respiratory and
756 cardiac data, RETROICOR may allow more targeted removal of physiological impacts to
757 decrease false positives (Glover et al., 2000; Bollmann et al., 2018).

758 A greater number of time points in multiband may allow more aggressive retrospective
759 motion correction using derivatives and quadratic terms of the motion parameters, scrub-

760 bing, and/or other approaches (Ciric et al., 2017; Power et al., 2014). However, many of
761 these methods can not be combined with simultaneous bandpass regression as the number
762 of predictors in the design matrix approaches or exceeds the number of time points. For ex-
763 ample, in our six minute acquisitions, including the 9 regressors, their derivatives, quadratic
764 terms, and squares of derivatives (36 p, Satterthwaite et al. 2013) leaves 10 or fewer residual
765 degrees of freedom for all acquisitions (see Table 1). Although the more aggressive noise
766 removal strategies can remove distance-dependent motion artifacts, the 9p pipeline had the
767 best network modularity quality (Ciric et al., 2017), which may be related to possible over-
768 fitting in aggressive approaches. Additionally, recent evidence suggests that changes in the
769 magnetic field caused by respiratory effects can falsely appear to be motion artifacts, which
770 results in overly aggressive frame censoring and data loss and can corrupt nuisance regressors
771 (Fair et al., 2020). We chose to use the same pipelines for all acquisitions to isolate the effect
772 of MB factor, rather than more aggressive noise removal strategies that are facilitated by
773 the acquisition of a larger number of volumes, but which may be removing false positives
774 and false negatives.

775 While retrospective image post-processing methods are commonly used to reduce motion
776 effects, prospective motion correction methods can be used to mitigate spin history effects.
777 Methods for multislice-to-volume registration that do not require external hardware have
778 been developed for real-time motion monitoring in multiband studies (Hoinkiss et al., 2019).
779 Higher temporal resolution associated with higher MB factor could carry additional benefits
780 in prospective motion correction but potentially have higher computational costs.

781 ICA-based artifact removal approaches may be more effective in multiband acquisitions;
782 however, noise amplification is a separate issue. ICA-AROMA can be used to estimate the
783 time courses of motion (Pruim et al., 2015), and ICA-FIX additionally estimates physiology
784 and some multiband artifacts (Griffanti et al., 2014). Multiband artifacts identified using
785 ICA-FIX have a “checkerboard” pattern (Griffanti et al., 2017). The corresponding indepen-
786 dent component time courses appear to correspond to motion and the interaction with the

787 slice-GRAPPA kernels. Mathematically, an IC component represents a spatial map with a
788 single time course. This approach may not be suited to capturing noise amplification because
789 the thermal noise time courses are not shared at different locations within the axial plane;
790 the noise has high rank that is not captured by a low-rank structure. As shown in Risk et al.
791 (2018), the ICA-FIX preprocessed resting-state fMRI in the Human Connectome Project still
792 contains large noise amplification, particularly in subcortical regions. In the present work,
793 correlations involving subcortical regions in the ICA-FIX HCP preprocessed data tended to
794 be weak (Web Supplement Figure S.15). We speculate that ICA-based artifact removal can
795 reduce motion and physiological artifacts, which can decrease spurious false positives, but
796 would not greatly impact noise amplification.

797 PCA-based data reduction, in which a signal subspace is estimated and the many direc-
798 tions of low variation are discarded, is another alternative cleaning strategy. This approach
799 may be similar to bandpass filtering. In particular, it may greatly reduce the noise but also
800 reduce the benefits of higher sampling rates. Although we speculate ICA artifact removal
801 would not address noise amplification, ICA-based functional connectivity analyses may re-
802 duce noise amplification, since ICA methods first apply a PCA-dimension reduction step.
803 PCA noise reduction is an important avenue for future research.

804 Another possible concern in multiband acquisitions is slice leakage artifacts and spurious
805 correlations. The original slice-GRAPPA algorithm resulted in signal leaking to aliased
806 locations, but this appears to have been largely addressed by split slice-GRAPPA (leak
807 block) reconstruction (Cauley et al., 2014; Todd et al., 2016; Risk et al., 2018). A related
808 issue may occur with thermal noise. The thermal noise shared by aliased locations resulted
809 in spurious correlations in the slice-GRAPPA reconstruction of rs-fMRI data in a simulation
810 study (Setsompop et al., 2013). However, our analyses demonstrate that correlations decrease
811 at higher multiband factors (Figure 5). Moreover, the correlations in Figure 2 are a single
812 axial slice at the center of the seed ROI, and thus there is no aliasing between voxels within
813 these seed maps. The impacts of slice separation on spurious correlations is understudied.

814 In particular, the impacts should be evaluated in recently proposed reconstruction methods
815 that are emerging as alternatives to split slice-GRAPPA (discussed below).

816 *5.5. Voxel size and other considerations*

817 In this study, our analysis used volume-based space with 2 mm MB data and 3.3 mm
818 SB data, whereas a surface-based analysis may provide different insights. An important
819 question raised by this is whether a 2 mm acquisition is beneficial when conducting volume-
820 based analyses, particularly if the primary interest is to study subcortical connectivity. Our
821 approach showed little advantage of smaller voxel size in the seed maps. There appears to
822 be fair specificity in gray matter regions in the SB 3.3 mm acquisition; for example, the
823 left and right insula are clearly delineated in the top row of Figure 3. The higher-resolution
824 associated with 2-mm isotropic voxel size could allow a better parcellation of small anatomical
825 structures such as sub-nuclei of the thalamus. Our analyses suggest these choices should be
826 evaluated in light of the dramatic reduction in effect sizes in the putamen and the thalamus
827 when using 2 mm compared to 3.3 mm. We elected to use a volume-based approach for
828 our primary analyses, since volume-based analyses are used for subcortical analyses, and
829 subcortical regions are prone to have lower SNR due to low coil sensitivity and high *g*-factor.
830 It is unknown how an MB 6 3.3 mm acquisition would compare to the SB 3.3 mm. Note
831 it is generally not feasible to map 3.3 mm voxels to the surface, and hence, a surface-based
832 analysis would be restricted to the 2 mm acquisitions.

833 We also examined the correlations between regions in the surface parcellation from
834 Glasser et al. (2016) using the surface-registered HCP data together with the nineteen non-
835 cortical gray matter volume-based regions (Web Supplement Figure S.15). Many of the
836 correlations involving subcortical regions were small. This is consistent with the hypothesis
837 that noise amplification results in spatial biases in correlations, although in this analysis
838 the size of the regions varied which can also impact the analysis. As in the Emory cohort,
839 subcortical functional connectivity was more prominent in the Cohen's d matrices. The costs
840 and benefits of voxel size, as well as volume versus surface-based representations of BOLD

841 signal, is also an important avenue for future research.

842 A comparison of the effect sizes in a 64-channel versus 32-channel head coil is not possible
843 in our study due to the small size of the University of Rochester cohort. [Seidel et al.](#)
844 ([2020](#)) found that temporal SNR was higher using a 64-channel versus 20-channel head coil
845 and recommended MB 6 with no in-plane acceleration, but 32-channel head coils were not
846 evaluated.

847 In line with the approach used in the HCP ([Ugurbil et al., 2013](#); [Xu et al., 2013](#)), we
848 did not use in-plane acceleration due to a concern with SNR loss and *g*-factor penalties. In-
849 plane acceleration leads to substantial SNR decrease ([Seidel et al., 2020](#)). Studies interested
850 in regions with severe magnetic-susceptibility induced distortion should cautiously balance
851 the benefits of in-plane acceleration and the loss in power.

852 We utilized split-slice GRAPPA for reconstruction ([Cauley et al., 2014](#)) implemented by
853 the CMRR sequences. However, recently introduced reconstruction methods may increase
854 the benefits of acceleration. Methods using convolutional neural networks are being devel-
855 oped ([Akçakaya et al., 2019](#); [Mickevicius et al., 2019](#); [Nencka et al., 2020](#)). [Chiew and Miller](#)
856 ([2019](#)) add a ridge penalty on the difference between time points to decrease noise amplifi-
857 cation and improve multiband reconstruction. These new developments may allow the use
858 of higher MB factors.

859 An important application of multiband acquisition is to studies of dynamic functional
860 connectivity. The Nyquist frequencies for MB 4, 6 and 8 are 0.34 Hz, 0.52 Hz, and 0.68
861 Hz, respectively, suggesting MB 8 will facilitate the detection of brain dynamics. However,
862 the ability of higher frequency data to resolve faster brain dynamics will also be impacted
863 by the noise characteristics of those acquisitions. Moreover, the spatial biases of multiband
864 acquisition may also impact dynamic connectivity studies.

865 **6. Conclusions**

866 In seed-based analyses of putamen functional connectivity and seed-based analyses of
867 motor-thalamic connectivity, we recommend SB 3.3 mm. MB 4 2 mm also revealed subcor-
868 tical connectivity, as well as motor-cerebellum connectivity, and is a good option for studies
869 desiring smaller voxel size. In effect sizes from correlation matrices using a brain-wide func-
870 tional atlas, MB 4, 6, and 8 had similar results. In general, MB 8 and higher did not have
871 advantages over MB 4 or 6. Overall, MB 4 is a reasonable choice for studies examining
872 both subcortical seed-based functional connectivity and brain-wide correlation matrices. We
873 recommend reporting Cohen's d or test statistics rather than correlations, as these measures
874 were less sensitive to the biases created by spatially heterogeneous noise amplification. Cor-
875 relations with 9p preprocessing without noise removal should not be reported. Bandpass
876 filtering can reduce noise amplification but also effect sizes, with the caveat that we do not
877 distinguish a reduction in physiology-based activation from a loss in neuronal activation in
878 the atlas-based analysis.

879 **7. Data and code availability statement**

880 The preprocessing and analysis pipelines used toolboxes and packages from FSL 6.0.3,
881 AFNI 19.3.16, Matlab R2020a, and R 3.6.0, with details described in Section [3 Methods](#).
882 Additionally, figures were created using wb_view in Connectome Workbench 1.4.2 ([Marcus](#)
883 [et al., 2011](#)) and BrainNet viewer 1.7 ([Xia et al., 2013](#)).

884 The Emory Multiband Dataset is available on OpenNeuro: <https://openneuro.org/datasets/ds003540>. Bash preprocessing, Matlab, and R scripts are available at the Brain
885 Research in Imaging Statistics Kit: <https://github.com/thebrisklab/RestingStateMultiband>.

887 **Declaration of Competing Interest**

888 None.

889 **Acknowledgments**

890 The authors thank Dr. Gopinath Kaundinya, Emory University, Dr. David Reiter, Emory
891 University, Dr. Allyson Mackey, University of Pennsylvania, and three anonymous reviewers
892 for helpful comments and discussions. We would like to thank Sarah Basadre, Michael Larch,
893 Sonny Roh, and Samira Yeboah for MRI acquisition and Lei Zhou for computational support.
894 Data collection in this study was supported by the Dean's Pilot and Innovation Grant of
895 the Rollins School of Public Health at Emory University to B.B.R. and the Center for
896 Systems Imaging Core Pilot Grant at Emory University to B.B.R. Analysis, interpretation,
897 and writing of the report were supported by NIH R21AG066970 to B.B.R., Z.Z., and D.Q.,
898 K01MH109766 to M.B.N, and P50AG025688 and R21AG064405 to D.Q.

899 **Appendix A. Power when comparing two groups**

900 Let $z_{avv'1}$ and $z_{avv'2}$ denote the population Fisher z-transformed correlation for groups
901 1 and 2, respectively. Assume N subjects for each group: $\hat{z}_{iavv'1} \stackrel{iid}{\sim} \mathcal{N}(z_{avv'1}, \nu_{avv'}^2)$ and
902 $\hat{z}_{iavv'2} \stackrel{iid}{\sim} \mathcal{N}(z_{avv'2}, \nu_{avv'}^2)$. In the one-sided test $H_0 : z_{avv'1} \leq z_{avv'2}$ and $H_a : z_{avv'1} > z_{avv'2}$,
903 the power is

$$\Phi \left(\sqrt{N} \frac{z_{avv'1} - z_{avv'2}}{\sqrt{2}\nu_{avv'}} - c_{1-\alpha} \right). \quad (\text{A.1})$$

904 By (3), $z_{avv'1}$ and $z_{avv'2}$ are attenuated by noise amplification, which can decrease statistical
905 power.

906 **Appendix B. Implications of autocorrelation on power**

907 Recall that $\hat{z}_{iavv'}$ is the sample correlation between locations v and v' for MB factor a in
908 subject i . Also recall that $\text{Var}(\hat{z}_{iavv'}) = \nu_{avv'}^2$. In the absence of autocorrelation, $1/\nu_{avv'}^2 \approx T_a$.
909 Let $1/\nu_{avv'}^2 = f_{avv'}(T_a, z_{avv'})$, where $f_{avv'}(\cdot, \cdot)$ is the function characterizing the impact of
910 autocorrelation in the two time series and their population correlation $z_{avv'}$ (here, Fisher

z-transformed). Related results and special cases for the untransformed correlations are in
 Davey et al. (2013), Fiecas et al. (2017), and Arbabshirani et al. (2014), but in general, this
 is a complicated function. Under positive autocorrelation, $f(T_a, z_{avv'}) \lesssim T_a$ (where we use
 the notation “ \lesssim ” because this is an asymptotic result that holds for sufficiently large T_a),
 with $f(T_a, z_{avv'}) \approx T_a$ when time series for both locations v and v' have zero autocorrelation.
 Using (3), the population effect size (Cohen’s d) is

$$d_{avv'} \approx \sqrt{f_{avv'}(T_a, z_{avv'})} \operatorname{arctanh} \left(\frac{\psi_{vv'}}{\sqrt{\sigma_v^2 + \eta_{av}^2} \sqrt{\sigma_{v'}^2 + \eta_{av'}^2}} \right). \quad (\text{B.1})$$

Then the power in (4) becomes $\Phi(\sqrt{N}d_{avv'} - c_{1-\alpha})$.

Inspecting (B.1), the term $\sqrt{f_{avv'}(T_a, z_{avv'})}$ can offset the increase in η_{av}^2 . Additionally, the function $f_{avv'}(T_a, z_{avv'})$ may vary across space. Bollmann et al. (2018) found the autoregressive coefficients tend to be lower in subcortical regions in task fMRI. Then the term $f_{avv'}(T_a, z_{avv'})$ may be closer to T_a in high noise amplification regions. Let $\bar{z}_{avv'} = \sum_i \hat{z}_{iavv'}/N$ and $sd(\hat{z}_{iavv'}) = \sqrt{\sum_i (\hat{z}_{iavv'} - \bar{z}_{avv'})^2/(N-1)}$, and define the sample Cohen’s d: $\hat{d}_{avv'} = \bar{z}_{avv'}/sd(\hat{z}_{iavv'})$. In practice, we expect $sd(\hat{z}_{iavv'})$ to be larger than $\sqrt{1/T}$ even if there is no autocorrelation due to violations of the assumption that all participants’ Fisher z-transformed correlations are realizations of the same population parameter $z_{avv'}$. To the extent that the model generating (B.1) captures key elements of the data, then $\hat{d}_{avv'}$ may be a useful measure of functional connectivity in MB acquisitions. Insight into temporal filtering can also be gained with this model. Temporal filtering reduces the effective degrees of freedom (Davey et al., 2013), resulting in $f_{avv'}(T_a, z_{avv'}) \ll T_a$, but can also increase the magnitude of correlations by reducing η_{av}^2 and $\eta_{av'}^2$.

Accurate modeling of autocorrelation is important in single-subject analysis of multiband task fMRI studies with short TR, with relatively minor impacts in group studies (Olszowy et al., 2019). Similarly, studies on the distribution of correlations have focused on single-subject analysis (James et al., 2019; Davey et al., 2013) with autocorrelation corrections

having little impact on group inference (Arbabshirani et al., 2014), although additional research in MB acquisitions would be useful. We note that prewhitening the time series, and closely related, using the residuals from models fitting the autocorrelation, can reduce $\nu_{avv'}^2$, but it can also impact $\psi_{vv'}$ in (1). The underlying vascular response to neural activity is also autocorrelated, and the hemodynamic response function follows a temporal pattern (Lindquist et al., 2009). Hence, applying a pre-whitening matrix may be undesirable. Pre-whitening in functional connectivity was not used in a number of prominent studies of functional connectivity nor is it a standard preprocessing step (Finn et al., 2015; Smith et al., 2013; Esteban et al., 2019). Hence, in our data application, we adapted a preprocessing pipeline that did not include prewhitening (Section 3.2 *FMRI data processing*).

Appendix C. Supplementary Materials

GFactorTables264nodes.xlsx includes tables of the apparent g -factors for the 9p and 9p+bandpass pipelines for the 264-node atlas.

WebSupplement_RestingStateFMRI_Multiband.pdf includes Web Supplement Figures S.1-S.15 and Tables S.1-S.5, including results from the University of Rochester cohort and secondary analysis of the HCP dataset.

References

- Akçakaya, M., Moeller, S., Weingärtner, S., and Uğurbil, K. (2019). Scan-specific robust artificial-neural-networks for k-space interpolation (RAKI) reconstruction: Database-free deep learning for fast imaging. *Magnetic Resonance in Medicine*, 81(1):439–453.
- Andersson, J. L., Skare, S., and Ashburner, J. (2003). How to correct susceptibility distortions in spin-echo echo-planar images: Application to diffusion tensor imaging. *NeuroImage*, 20(2):870–888.
- Arbabshirani, M. R., Damaraju, E., Phlypo, R., Plis, S., Allen, E., Ma, S., Mathalon, D.,

- 959 Preda, A., Vaidya, J. G., Adali, T., and Calhoun, V. D. (2014). Impact of autocorrelation
960 on functional connectivity. *NeuroImage*, 102(P2):294–308.
- 961 Bastian, A. J. and Thach, W. T. (1995). Cerebellar outflow lesions: A comparison of
962 movement deficits resulting from lesions at the levels of the cerebellum and thalamus.
963 *Annals of Neurology*.
- 964 Bhandari, R., Kirilina, E., Caan, M., Suttrup, J., de Sanctis, T., De Angelis, L., Keysers,
965 C., and Gazzola, V. (2019). Does higher sampling rate (Multiband + SENSE) benefit the
966 detection of task correlated BOLD for cognitive neuroscience applications at 3T? *bioRxiv*,
967 page 762831.
- 968 Biswal, B., Zerrin Yetkin, F., Haughton, V. M., and Hyde, J. S. (1995). Functional con-
969 nectivity in the motor cortex of resting human brain using echo-planar mri. *Magnetic*
970 *Resonance in Medicine*.
- 971 Biswal, B. B., Mennes, M., Zuo, X. N., Gohel, S., Kelly, C., Smith, S. M., Beckmann, C. F.,
972 Adelstein, J. S., Buckner, R. L., Colcombe, S., and others (2010). Toward discovery science
973 of human brain function. *Proceedings of the National Academy of Sciences*, 107(10):4734–
974 4739.
- 975 Bollmann, S., Puckett, A. M., Cunnington, R., and Barth, M. (2018). Serial correlations in
976 single-subject fMRI with sub-second TR. *NeuroImage*, 166:152–166.
- 977 Boyacioglu, R., Schulz, J., Koopmans, P. J., Barth, M., and Norris, D. G. (2015). Improved
978 sensitivity and specificity for resting state and task fMRI with multiband multi-echo EPI
979 compared to multi-echo EPI at 7T. *Neuroimage*, 119:352–361.
- 980 Breuer, F. A., Kannengiesser, S. A., Blaimer, M., Seiberlich, N., Jakob, P. M., and Griswold,
981 M. A. (2009). General formulation for quantitative G-factor calculation in GRAPPA
982 reconstructions. *Magnetic Resonance in Medicine*, 62(3):739–746.

- 983 Bright, M. G., Tench, C. R., and Murphy, K. (2017). Potential pitfalls when denoising
984 resting state fMRI data using nuisance regression. *NeuroImage*, 154:159–168.
- 985 Buckner, R. L., Krienen, F. M., Castellanos, A., Diaz, J. C., and Thomas Yeo, B. T. (2011).
986 The organization of the human cerebellum estimated by intrinsic functional connectivity.
987 *Journal of Neurophysiology*, 106(5):2322–2345.
- 988 Cauley, S. F., Polimeni, J. R., Bhat, H., Wald, L. L., and Setsompop, K. (2014). Interslice
989 leakage artifact reduction technique for simultaneous multislice acquisitions. *Magnetic
990 Resonance in Medicine*, 72(1):93–102.
- 991 Cerliani, L., Mennes, M., Thomas, R. M., Di Martino, A., Thioux, M., and Keysers, C.
992 (2015). Increased functional connectivity between subcortical and cortical resting-state
993 networks in Autism spectrum disorder. *JAMA Psychiatry*.
- 994 Chand, G. B., Wu, J., Hajjar, I., and Qiu, D. (2017). Interactions of the Salience Network
995 and Its Subsystems with the Default-Mode and the Central-Executive Networks in Normal
996 Aging and Mild Cognitive Impairment. *Brain Connectivity*, 7(7):401–412.
- 997 Chen, J. C., Forsyth, A., Dubowitz, D. J., and Muthukumaraswamy, S. D. (2020). On
998 the Quality, Statistical Efficiency, and Safety of Simultaneously Recorded Multiband
999 fMRI/EEG. *Brain Topography*, 33(3):303–316.
- 1000 Chen, J. E., Polimeni, J. R., Bollmann, S., and Glover, G. H. (2019). On the analysis of
1001 rapidly sampled fMRI data. *NeuroImage*, 188:807–820.
- 1002 Chen, L., Vu, A. T., Xu, J., Moeller, S., Ugurbil, K., Yacoub, E., and Feinberg, D. A. (2015).
1003 Evaluation of highly accelerated simultaneous multi-slice EPI for fMRI. *Neuroimage*,
1004 104:452–459.
- 1005 Chiew, M. and Miller, K. L. (2019). Improved statistical efficiency of simultaneous multi-

- 1006 slice fMRI by reconstruction with spatially adaptive temporal smoothing. *NeuroImage*,
1007 203:116165.
- 1008 Ciric, R., Wolf, D. H., Power, J. D., Roalf, D. R., Baum, G. L., Ruparel, K., Shinohara,
1009 R. T., Elliott, M. A., Eickhoff, S. B., Davatzikos, C., Gur, R. C., Gur, R. E., Bassett,
1010 D. S., and Satterthwaite, T. D. (2017). Benchmarking of participant-level confound re-
1011 gression strategies for the control of motion artifact in studies of functional connectivity.
1012 *NeuroImage*, 154:174–187.
- 1013 Cox, R. W. (1996). AFNI: Software for analysis and visualization of functional magnetic
1014 resonance neuroimages. *Computers and Biomedical Research*, 29(3):162–173.
- 1015 Davey, C. E., Grayden, D. B., Egan, G. F., and Johnston, L. A. (2013). Filtering induces
1016 correlation in fMRI resting state data. *NeuroImage*, 64(1):728–740.
- 1017 Demetriou, L., Kowalczyk, O. S., Tyson, G., Bello, T., Newbould, R. D., and Wall, M. B.
1018 (2018). A comprehensive evaluation of increasing temporal resolution with multiband-
1019 accelerated protocols and effects on statistical outcome measures in fMRI. *NeuroImage*,
1020 176:404–416.
- 1021 Di Martino, A., Kelly, C., Grzadzinski, R., Zuo, X. N., Mennes, M., Mairena, M. A., Lord,
1022 C., Castellanos, F. X., and Milham, M. P. (2011). Aberrant striatal functional connectivity
1023 in children with autism. *Biological Psychiatry*, 69(9):847–856.
- 1024 Dum, R. P. and Strick, P. L. (2003). An unfolded map of the cerebellar dentate nucleus and
1025 its projections to the cerebral cortex. *Journal of Neurophysiology*, 89(1):634–639.
- 1026 Esteban, O., Markiewicz, C. J., Blair, R. W., Moodie, C. A., Isik, A. I., Erramuzpe, A., Kent,
1027 J. D., Goncalves, M., DuPre, E., Snyder, M., Oya, H., Ghosh, S. S., Wright, J., Durnez,
1028 J., Poldrack, R. A., and Gorgolewski, K. J. (2019). fMRIprep: a robust preprocessing
1029 pipeline for functional MRI. *Nature Methods*, 16(1):111–116.

- 1030 Fair, D. A., Miranda-Dominguez, O., Snyder, A. Z., Perrone, A., Earl, E. A., Van, A. N.,
1031 Koller, J. M., Feczko, E., Tisdall, M. D., van der Kouwe, A., Klein, R. L., Mirro, A. E.,
1032 Hampton, J. M., Adeyemo, B., Laumann, T. O., Gratton, C., Greene, D. J., Schlaggar,
1033 B. L., Hagler, D. J., Watts, R., Garavan, H., Barch, D. M., Nigg, J. T., Petersen, S. E.,
1034 Dale, A. M., Feldstein-Ewing, S. W., Nagel, B. J., and Dosenbach, N. U. (2020). Correction
1035 of respiratory artifacts in MRI head motion estimates. *NeuroImage*, 208:116400.
- 1036 Feinberg, D. A., Moeller, S., Smith, S. M., Auerbach, E., Ramanna, S., Glasser, M. F.,
1037 Miller, K. L., Ugurbil, K., and Yacoub, E. (2010). Multiplexed echo planar imaging for
1038 sub-second whole brain {fMRI} and fast diffusion imaging. *PLoS one*, 5(12):e15710.
- 1039 Feinberg, D. A. and Setsompop, K. (2013). Ultra-fast MRI of the human brain with simul-
1040 taneous multi-slice imaging. *Journal of magnetic resonance*, 229:90–100.
- 1041 Fiecas, M., Cribben, I., Bahktiari, R., and Cummine, J. (2017). A variance components
1042 model for statistical inference on functional connectivity networks. *NeuroImage*, 149:256–
1043 266.
- 1044 Finn, E. S., Shen, X., Scheinost, D., Rosenberg, M. D., Huang, J., Chun, M. M., Pa-
1045 pademetris, X., and Constable, R. T. (2015). Functional connectome fingerprinting: iden-
1046 tifying individuals using patterns of brain connectivity. *Nature neuroscience*, 18(11):1664.
- 1047 Fox, M. D., Snyder, A. Z., Vincent, J. L., Corbetta, M., Van Essen, D. C., and Raichle,
1048 M. E. (2005). The human brain is intrinsically organized into dynamic, anticorrelated
1049 functional networks. *Proceedings of the National Academy of Sciences of the United States
1050 of America*, 102(27):9673–9678.
- 1051 Fox, M. D., Zhang, D., Snyder, A. Z., and Raichle, M. E. (2009). The global signal
1052 and observed anticorrelated resting state brain networks. *Journal of Neurophysiology*,
1053 101(6):3270–3283.

- 1054 Glasser, M. F., Coalson, T. S., Robinson, E. C., Hacker, C. D., Harwell, J., Yacoub, E.,
1055 Ugurbil, K., Andersson, J., Beckmann, C. F., Jenkinson, M., and others (2016). A multi-
1056 modal parcellation of human cerebral cortex. *Nature*, 536(7615):171–178.
- 1057 Glasser, M. F., Sotiropoulos, S. N., Wilson, J. A., Coalson, T. S., Fischl, B., Andersson,
1058 J. L., Xu, J., Jbabdi, S., Webster, M., Polimeni, J. R., and others (2013). The minimal
1059 preprocessing pipelines for the Human Connectome Project. *NeuroImage*, 80:105–124.
- 1060 Glover, G. H., Li, T., and Ress, D. (2000). Image-based method for retrospective correction
1061 of physiological motion effects in fMRI: RETROICOR. *Magnetic Resonance in Medicine*,
1062 44(1):162–167.
- 1063 Greicius, M. (2008). Resting-state functional connectivity in neuropsychiatric disorders.
1064 *Current Opinion in Neurology*, 21(4):424–430.
- 1065 Greicius, M. D., Flores, B. H., Menon, V., Glover, G. H., Solvason, H. B., Kenna, H., Reiss,
1066 A. L., and Schatzberg, A. F. (2007). Resting-State Functional Connectivity in Major
1067 Depression: Abnormally Increased Contributions from Subgenual Cingulate Cortex and
1068 Thalamus. *Biological Psychiatry*, 62(5):429–437.
- 1069 Griffanti, L., Douaud, G., Bijsterbosch, J., Evangelisti, S., Alfaro-Almagro, F., Glasser,
1070 M. F., Duff, E. P., Fitzgibbon, S., Westphal, R., Carone, D., and others (2017). Hand
1071 classification of fMRI ICA noise components. *Neuroimage*, 154:188–205.
- 1072 Griffanti, L., Salimi-Khorshidi, G., Beckmann, C. F., Auerbach, E. J., Douaud, G., Sexton,
1073 C. E., Zsoldos, E., Ebmeier, K. P., Filippini, N., Mackay, C. E., and others (2014). ICA-
1074 based artefact removal and accelerated fMRI acquisition for improved resting state network
1075 imaging. *NeuroImage*, 95:232–247.
- 1076 Haber, S. N. and Calzavara, R. (2009). The cortico-basal ganglia integrative network: The
1077 role of the thalamus.

- 1078 Haber, S. N., Kim, K. S., Mailly, P., and Calzavara, R. (2006). Reward-related cortical
1079 inputs define a large striatal region in primates that interface with associative cortical
1080 connections, providing a substrate for incentive-based learning. *Journal of Neuroscience*,
1081 26(32).
- 1082 Hagler, D. J., Hatton, S. N., Cornejo, M. D., Makowski, C., Fair, D. A., Dick, A. S.,
1083 Sutherland, M. T., Casey, B. J., Barch, D. M., Harms, M. P., Watts, R., Bjork, J. M.,
1084 Garavan, H. P., Hilmer, L., Pung, C. J., Sicat, C. S., Kuperman, J., Bartsch, H., Xue, F.,
1085 Heitzeg, M. M., Laird, A. R., Trinh, T. T., Gonzalez, R., Tapert, S. F., Riedel, M. C.,
1086 Squeglia, L. M., Hyde, L. W., Rosenberg, M. D., Earl, E. A., Howlett, K. D., Baker, F. C.,
1087 Soules, M., Diaz, J., de Leon, O. R., Thompson, W. K., Neale, M. C., Herting, M., Sowell,
1088 E. R., Alvarez, R. P., Hawes, S. W., Sanchez, M., Bodurka, J., Breslin, F. J., Morris, A. S.,
1089 Paulus, M. P., Simmons, W. K., Polimeni, J. R., van der Kouwe, A., Nencka, A. S., Gray,
1090 K. M., Pierpaoli, C., Matochik, J. A., Noronha, A., Aklin, W. M., Conway, K., Glantz,
1091 M., Hoffman, E., Little, R., Lopez, M., Pariyadath, V., Weiss, S. R., Wolff-Hughes, D. L.,
1092 DelCarmen-Wiggins, R., Feldstein Ewing, S. W., Miranda-Dominguez, O., Nagel, B. J.,
1093 Perrone, A. J., Sturgeon, D. T., Goldstone, A., Pfefferbaum, A., Pohl, K. M., Prouty, D.,
1094 Uban, K., Bookheimer, S. Y., Dapretto, M., Galvan, A., Bagot, K., Giedd, J., Infante,
1095 M. A., Jacobus, J., Patrick, K., Shilling, P. D., Desikan, R., Li, Y., Sugrue, L., Banich,
1096 M. T., Friedman, N., Hewitt, J. K., Hopfer, C., Sakai, J., Tanabe, J., Cottler, L. B., Nixon,
1097 S. J., Chang, L., Cloak, C., Ernst, T., Reeves, G., Kennedy, D. N., Heeringa, S., Peltier,
1098 S., Schulenberg, J., Sripada, C., Zucker, R. A., Iacono, W. G., Luciana, M., Calabro, F. J.,
1099 Clark, D. B., Lewis, D. A., Luna, B., Schirda, C., Brima, T., Foxe, J. J., Freedman, E. G.,
1100 Mruzek, D. W., Mason, M. J., Huber, R., McGlade, E., Prescott, A., Renshaw, P. F.,
1101 Yurgelun-Todd, D. A., Allgaier, N. A., Dumas, J. A., Ivanova, M., Potter, A., Florsheim,
1102 P., Larson, C., Lisdahl, K., Charness, M. E., Fuemmeler, B., Hettema, J. M., Maes, H. H.,
1103 Steinberg, J., Anokhin, A. P., Glaser, P., Heath, A. C., Madden, P. A., Baskin-Sommers,
1104 A., Constable, R. T., Grant, S. J., Dowling, G. J., Brown, S. A., Jernigan, T. L., and Dale,

- 1105 A. M. (2019). Image processing and analysis methods for the Adolescent Brain Cognitive
1106 Development Study. *NeuroImage*, 202:116091.
- 1107 Halekoh, U., Højsgaard, S., and Yan, J. (2006). The R Package geepack for Generalized
1108 Estimating Equations. Technical Report 2.
- 1109 Hallquist, M. N., Hwang, K., and Luna, B. (2013). The nuisance of nuisance regression:
1110 Spectral misspecification in a common approach to resting-state fMRI preprocessing rein-
1111 troduces noise and obscures functional connectivity. *NeuroImage*, 82:208–225.
- 1112 Hoinkiss, D. C., Erhard, P., Breutigam, N. J., von Samson-Himmelstjerna, F., Günther,
1113 M., and Porter, D. A. (2019). Prospective motion correction in functional MRI using
1114 simultaneous multislice imaging and multislice-to-volume image registration. *NeuroImage*,
1115 200:159–173.
- 1116 Howell, B. R., Styner, M. A., Gao, W., Yap, P. T., Wang, L., Baluyot, K., Yacoub, E.,
1117 Chen, G., Potts, T., Salzwedel, A., Li, G., Gilmore, J. H., Piven, J., Smith, J. K., Shen,
1118 D., Ugurbil, K., Zhu, H., Lin, W., and Elison, J. T. (2019). The UNC/UMN Baby
1119 Connectome Project (BCP): An overview of the study design and protocol development.
- 1120 Jahanian, H., Holdsworth, S., Christen, T., Wu, H., Zhu, K., Kerr, A. B., Middione, M. J.,
1121 Dougherty, R. F., Moseley, M., and Zaharchuk, G. (2019). Advantages of short repetition
1122 time resting-state functional MRI enabled by simultaneous multi-slice imaging. *Journal
1123 of Neuroscience Methods*, 311:122–132.
- 1124 James, O., Park, H., and Kim, S. (2019). Impact of sampling rate on statistical significance
1125 for single subject fMRI connectivity analysis. *Human Brain Mapping*, 40(11):3321–3337.
- 1126 Jenkinson, M., Bannister, P., Brady, M., and Smith, S. (2002). Improved Optimization for
1127 the Robust and Accurate Linear Registration and Motion Correction of Brain Images.
1128 *NeuroImage*.

- 1129 Konova, A. B., Moeller, S. J., Tomasi, D., Volkow, N. D., and Goldstein, R. Z. (2013). Ef-
1130 ffects of methylphenidate on resting-state functional connectivity of the mesocorticolimbic
1131 dopamine pathways in cocaine addiction. *JAMA Psychiatry*.
- 1132 Kravitz, A. V., Freeze, B. S., Parker, P. R., Kay, K., Thwin, M. T., Deisseroth, K., and
1133 Kreitzer, A. C. (2010a). Regulation of parkinsonian motor behaviours by optogenetic
1134 control of basal ganglia circuitry. *Nature*.
- 1135 Kravitz, A. V., Freeze, B. S., Parker, P. R. L., Kay, K., Myo, T., Deisseroth, K., and Kreitzer,
1136 A. C. (2010b). Control of Basal Ganglia Circuitry. *Nature*, 466(7306):622–626.
- 1137 Lee, H. L., Zahneisen, B., Hugger, T., LeVan, P., and Hennig, J. (2013). Tracking dy-
1138 namic resting-state networks at higher frequencies using MR-encephalography. *NeuroIm-*
1139 *age*, 65:216–222.
- 1140 Lindquist, M. A., Geuter, S., Wager, T. D., and Caffo, B. S. (2019). Modular preprocessing
1141 pipelines can reintroduce artifacts into fMRI data. *Human Brain Mapping*, 40(8):2358–
1142 2376.
- 1143 Lindquist, M. A., Meng Loh, J., Atlas, L. Y., and Wager, T. D. (2009). Modeling the
1144 hemodynamic response function in fMRI: efficiency, bias and mis-modeling. *NeuroImage*,
1145 45(1 Suppl).
- 1146 Marcus, D. S., Harwell, J., Olsen, T., Hodge, M., Glasser, M. F., Prior, F., Jenkinson, M.,
1147 Laumann, T., Curtiss, S. W., and Van Essen, D. C. (2011). Informatics and Data Mining
1148 Tools and Strategies for the Human Connectome Project. *Frontiers in Neuroinformatics*,
1149 5:4.
- 1150 Mickevicius, N. J., Paulson, E. S., Muftuler, L. T., and Nencka, A. S. (2019). Application of
1151 a k-Space Interpolating Artificial Neural Network to In-Plane Accelerated Simultaneous
1152 Multislice Imaging.

- 1153 Miller, K. L., Alfaro-Almagro, F., Bangerter, N. K., Thomas, D. L., Yacoub, E., Xu, J.,
1154 Bartsch, A. J., Jbabdi, S., Sotiroopoulos, S. N., Andersson, J. L., Griffanti, L., Douaud, G.,
1155 Okell, T. W., Weale, P., Dragonu, I., Garratt, S., Hudson, S., Collins, R., Jenkinson, M.,
1156 Matthews, P. M., and Smith, S. M. (2016a). Multimodal population brain imaging in the
1157 UK Biobank prospective epidemiological study. *Nature Neuroscience*, 19(11):1523–1536.
- 1158 Miller, K. L., Alfaro-Almagro, F., Bangerter, N. K., Thomas, D. L., Yacoub, E., Xu, J.,
1159 Bartsch, A. J., Jbabdi, S., Sotiroopoulos, S. N., Andersson, J. L. R., and others (2016b).
1160 Multimodal population brain imaging in the UK Biobank prospective epidemiological
1161 study. *Nature Neuroscience*.
- 1162 Moeller, S., Yacoub, E., Olman, C. A., Auerbach, E., Strupp, J., Harel, N., and Ugurbil, K.
1163 (2010). Multiband multislice GE-EPI at 7 tesla, with 16-fold acceleration using partial
1164 parallel imaging with application to high spatial and temporal whole-brain fMRI. *Magnetic*
1165 *Resonance in Medicine*, 63(5):1144–1153.
- 1166 Nencka, A. S., PhD, Arpinar, V. E., PhD, Bhave, S., PhD, Yang, B., PhD, Banerjee, S.,
1167 McCrea, M., PhD, Mickevicius, N. J., Muftuler, L. T., and Koch, K. M. (2020). Split Slice
1168 Training Augmentation and Hyperparameter Tuning of RAKI Networks for Simultaneous
1169 Multi-Slice Reconstruction.
- 1170 Olszowy, W., Aston, J., Rua, C., and Williams, G. B. (2019). Accurate autocorrelation
1171 modeling substantially improves fMRI reliability. *Nature Communications*, 10(1):1–11.
- 1172 Parkes, L., Fulcher, B., Yücel, M., and Fornito, A. (2018). An evaluation of the efficacy,
1173 reliability, and sensitivity of motion correction strategies for resting-state functional MRI.
1174 *NeuroImage*, 171.
- 1175 Pessiglione, M., Seymour, B., Flandin, G., Dolan, R. J., and Frith, C. D. (2006). Dopamine-
1176 dependent prediction errors underpin reward-seeking behaviour in humans. *Nature*.

- 1177 Poldrack, R. A., Clark, J., Paré-Bлагoev, E. J., Shohamy, D., Crespo Moyano, J., Myers, C.,
1178 and Gluck, M. A. (2001). Interactive memory systems in the human brain. *Nature*.
- 1179 Power, J. D., Cohen, A. L., Nelson, S. M., Wig, G. S., Barnes, K. A., Church, J. A., Vogel,
1180 A. C., Laumann, T. O., Miezin, F. M., Schlaggar, B. L., and Petersen, S. E. (2011).
1181 Functional Network Organization of the Human Brain. *Neuron*, 72(4):665–678.
- 1182 Power, J. D., Lynch, C. J., Adeyemo, B., and Petersen, S. E. (2020). A Critical,
1183 Event-Related Appraisal of Denoising in Resting-State fMRI Studies. *Cerebral Cortex*,
1184 30(10):5544–5559.
- 1185 Power, J. D., Lynch, C. J., Gilmore, A. W., Gotts, S. J., and Martin, A. (2019). Reply
1186 to Spreng et al.: Multiecho fMRI denoising does not remove global motion-associated
1187 respiratory signals.
- 1188 Power, J. D., Mitra, A., Laumann, T. O., Snyder, A. Z., Schlaggar, B. L., and Petersen,
1189 S. E. (2014). Methods to detect, characterize, and remove motion artifact in resting state
1190 fMRI. *NeuroImage*, 84:320–341.
- 1191 Power, J. D., Plitt, M., Laumann, T. O., and Martin, A. (2017). Sources and implications
1192 of whole-brain fMRI signals in humans. *NeuroImage*, 146.
- 1193 Preibisch, C., Bührer, M., Riedl, V., and others (2015). Evaluation of multiband EPI acqui-
1194 sitions for resting state fMRI. *PloS one*, 10(9):e0136961.
- 1195 Pruim, R. H., Mennes, M., van Rooij, D., Llera, A., Buitelaar, J. K., and Beckmann, C. F.
1196 (2015). ICA-AROMA: A robust ICA-based strategy for removing motion artifacts from
1197 fMRI data. *NeuroImage*, 112:267–277.
- 1198 Risk, B., Kociuba, M., and Rowe, D. (2018). Impacts of simultaneous multislice acquisition
1199 on sensitivity and specificity in fMRI. *NeuroImage*, 172.

- 1200 Satterthwaite, T. D., Elliott, M. A., Gerraty, R. T., Ruparel, K., Loughead, J., Calkins,
1201 M. E., Eickhoff, S. B., Hakonarson, H., Gur, R. C., Gur, R. E., and others (2013). An
1202 improved framework for confound regression and filtering for control of motion artifact in
1203 the preprocessing of resting-state functional connectivity data. *Neuroimage*, 64:240–256.
- 1204 Seidel, P., Levine, S. M., Tahedl, M., and Schwarzbach, J. V. (2020). Temporal Signal-to-
1205 Noise Changes in Combined Multislice- and In-Plane-Accelerated Echo-Planar Imaging
1206 with a 20- and 64-Channel Coil. *Scientific Reports*, 10(5536).
- 1207 Setsompop, K., Gagoski, B. A., Polimeni, J. R., Witzel, T., Wedeen, V. J., and Wald,
1208 L. L. (2012). Blipped-controlled aliasing in parallel imaging for simultaneous multislice
1209 echo planar imaging with reduced g-factor penalty. *Magnetic Resonance in Medicine*,
1210 67(5):1210–1224.
- 1211 Setsompop, K. P., J. R. Polimeni, Bhat, H., and Wald, L. L. (2013). Characterization of arti-
1212 factual correlation in highly-accelerated simultaneous multi-slice (SMS) fMRI acquisitions.
1213 Abstract 0410. In *ISMRM Proceedings*.
- 1214 Smith, S. M., Beckmann, C. F., Andersson, J., Auerbach, E. J., Bijsterbosch, J., Douaud,
1215 G., Duff, E., Feinberg, D. A., Griffanti, L., Harms, M. P., and others (2013). Resting-state
1216 fMRI in the human connectome project. *Neuroimage*, 80:144–168.
- 1217 Smith, S. M., Jenkinson, M., Woolrich, M. W., Beckmann, C. F., Behrens, T. E., Johansen-
1218 Berg, H., Bannister, P. R., De Luca, M., Drobniak, I., Flitney, D. E., Niazy, R. K.,
1219 Saunders, J., Vickers, J., Zhang, Y., De Stefano, N., Brady, J. M., and Matthews, P. M.
1220 (2004). Advances in functional and structural MR image analysis and implementation as
1221 FSL. In *NeuroImage*, volume 23. Neuroimage.
- 1222 Todd, N., Josephs, O., Zeidman, P., Flandin, G., Moeller, S., and Weiskopf, N. (2017).
1223 Functional sensitivity of 2D simultaneous multi-slice echo-planar imaging: effects of accel-
1224 eration on g-factor and physiological noise. *Frontiers in Neuroscience*, 11.

- 1225 Todd, N., Moeller, S., Auerbach, E. J., Yacoub, E., Flandin, G., and Weiskopf, N. (2016).
1226 Evaluation of 2D multiband EPI imaging for high-resolution, whole-brain, task-based fMRI
1227 studies at 3T: Sensitivity and slice leakage artifacts. *NeuroImage*, 124:32–42.
- 1228 Tsay, R. S. (2010). *Analysis of Financial Time Series Second Edition*. Wiley, 3rd edition.
- 1229 Ugurbil, K., Xu, J., Auerbach, E. J., Moeller, S., Vu, A. T., Duarte-Carvajalino, J. M.,
1230 Lenglet, C., Wu, X., Schmitter, S., de Moortele, P. F., and others (2013). Pushing spatial
1231 and temporal resolution for functional and diffusion MRI in the Human Connectome
1232 Project. *NeuroImage*, 80:80–104.
- 1233 Weiner, M. W., Veitch, D. P., Aisen, P. S., Beckett, L. A., Cairns, N. J., Green, R. C.,
1234 Harvey, D., Jack, C. R., Jagust, W., Morris, J. C., Petersen, R. C., Salazar, J., Saykin,
1235 A. J., Shaw, L. M., Toga, A. W., and Trojanowski, J. Q. (2017a). The Alzheimer’s Disease
1236 Neuroimaging Initiative 3: Continued innovation for clinical trial improvement.
- 1237 Weiner, M. W., Veitch, D. P., Aisen, P. S., Beckett, L. A., Cairns, N. J., Green, R. C.,
1238 Harvey, D., Jack, C. R., Jagust, W., Morris, J. C., Petersen, R. C., Salazar, J., Saykin,
1239 A. J., Shaw, L. M., Toga, A. W., and Trojanowski, J. Q. (2017b). The Alzheimer’s Disease
1240 Neuroimaging Initiative 3: Continued innovation for clinical trial improvement.
- 1241 Wood, S. (2017). *Generalized additive models: an introduction with R*. CRC Press.
- 1242 Woodward, N. D. and Heckers, S. (2016). Mapping Thalamocortical Functional Connectivity
1243 in Chronic and Early Stages of Psychotic Disorders. *Biological Psychiatry*, 79(12):1016–
1244 1025.
- 1245 Xia, M., Wang, J., and He, Y. (2013). BrainNet Viewer: A Network Visualization Tool for
1246 Human Brain Connectomics. *PLoS ONE*, 8(7).
- 1247 Xu, J., Moeller, S., Auerbach, E. J., Strupp, J., Smith, S. M., Feinberg, D. A., Yacoub,

₁₂₄₈ E., and Ugurbil, K. (2013). Evaluation of slice accelerations using multiband echo planar
₁₂₄₉ imaging at 3T. *NeuroImage*, 83:991–1001.